

A multiwavelength study of the debris disc around 49 Cet

Nicole Pawellek^{1,2}*, Attila Moór,² Julien Milli,³ Ágnes Kóspál,^{1,2}
 Johan Olofsson,^{1,4,5} Péter Ábrahám,² Miriam Keppler,¹ Quentin Kral^{1,6}, Adriana Pohl,¹
 Jean-Charles Augereau,⁷ Anthony Boccaletti,⁶ Gaël Chauvin,⁸ Élodie Choquet,⁹
 Natalia Engler,¹⁰ Thomas Henning,¹ Maud Langlois,¹¹ Eve J. Lee¹²,
 François Ménard,⁷ Philippe Thébault⁶ and Alice Zurlo^{13,14,15}

¹Max-Planck-Institut für Astronomie, Königstuhl 17, D-69117 Heidelberg, Germany

²Konkoly Observatory, Research Centre for Astronomy and Earth Sciences, Hungarian Academy of Sciences, Konkoly-Thege Miklós út 15-17, H-1121 Budapest, Hungary

³European Southern Observatory (ESO), Alonso de Córdova 3107, Vitacura, Casilla 19001, Santiago, Chile

⁴Instituto de Física y Astronomía, Facultad de Ciencias, Universidad de Valparaíso, Av. Gran Bretaña 1111, Playa Ancha, Valparaíso, Chile

⁵Núcleo Milenio Formación Planetaria – NPF, Universidad de Valparaíso, Av. Gran Bretaña 1111, Valparaíso, Chile

⁶LESIA, Observatoire de Paris, Université PSL, CNRS, Sorbonne Université, Univ. Paris Diderot, Sorbonne Paris Cité, 5 Place Jules Janssen, F-92195 Meudon, France

⁷Univ. Grenoble Alpes, CNRS, IPAG, F-38000 Grenoble, France

⁸International Franco-Chilean Laboratory of Astronomy, CNRS/INSU UMI3386, Department of Astronomy, University of Chile, Casilla 36-D, Santiago, Chile

⁹Aix Marseille Univ., CNRS CNES, LAM, Pôle de l'Étoile Site de Château-Gombert 38, rue Frédéric Joliot-Curie, F-13388 Marseille CEDEX 13, FRANCE

¹⁰ETH Zurich, Institute for Particle Physics and Astrophysics, Wolfgang-Pauli-Straße 27, CH-8093 Zurich, Switzerland

¹¹CRAL, UMR 5574, CNRS, Université Lyon 1, 9 avenue Charles André, F-69561 Saint Genis Laval CEDEX, France

¹²TAPIR, Walter Burke Institute for Theoretical Physics, Mailcode 350-17 Caltech, Pasadena, CA 91125, USA

¹³Núcleo de Astronomía, Facultad de Ingeniería y Ciencias, Universidad Diego Portales, Av. Ejército 441, Santiago, Chile

¹⁴Escuela de Ingeniería Industrial, Facultad de Ingeniería y Ciencias, Universidad Diego Portales, Av. Ejército 441, Santiago, Chile

¹⁵Aix Marseille Université, CNRS, LAM – Laboratoire d'Astrophysique de Marseille, UMR 7326, F-13388 Marseille, France

Accepted 2019 July 12. Received 2019 July 5; in original form 2019 March 12

ABSTRACT

In a multiwavelength study of thermal emission and scattered light images we analyse the dust properties and structure of the debris disc around the A1-type main-sequence star 49 Cet. As a basis for this study, we present new scattered light images of the debris disc known to possess a high amount of both dust and gas. The outer region of the disc is revealed in former coronagraphic *H*-band and our new *Y*-band images from the Very Large Telescope SPHERE instrument. We use the knowledge of the disc's radial extent inferred from ALMA observations and the grain size distribution found by spectral energy distribution fitting to generate semidynamical dust models of the disc. We compare the models to scattered light and thermal emission data and find that a disc with a maximum surface density at 110 au and shallow edges can describe both the thermal emission and the scattered light observations. This suggests that grains close to the blow-out limit and large grains stem from the same planetesimal population and are mainly influenced by radiation pressure. The influence of inward transport processes could not be analysed in this study.

Key words: circumstellar matter – stars: individual: 49 Cet – infrared: stars.

1 INTRODUCTION

Circumstellar discs around young stars are natural byproducts of star formation. They serve as a reservoir for mass accretion when

protostars form and afterwards transform to places where planets can form. At the beginning of their evolution, primordial discs are mostly composed of gas and only a minor mass fraction is present in small solid dust particles. The gas plays a major role in controlling the disc dust dynamics (Beckwith, Henning & Nakagawa 2000). Due to viscous accretion (Lynden-Bell & Pringle 1974) and photoevaporation (Alexander, Clarke & Pringle 2006)

* E-mail: pawellek@mpia.de

the gas is removed during the discs' evolution process and is mostly depleted during the first ~ 10 Myr (e.g. Zuckerman, Forveille & Kastner 1995; Fedele et al. 2010).

After this evolutionary phase, the dynamics of dust particles, being no longer governed or stabilized by the gas, are strongly influenced by stellar radiation pressure and Poynting–Robertson drag. In such an environment the lifetime of grains is much shorter than the lifetime of the host star (e.g. Dominik & Decin 2003; Wyatt 2005). In the last decades observations at infrared wavelengths revealed hundreds of dust-dominated discs around stars with a wide range of ages (Hughes, Duchêne & Matthews 2018). Considering the limited lifetime, the dust material of these *debris discs* could not be left over from the primordial stage but could rather comprise second-generation particles continuously replenishing from collisions and evaporation of previously formed larger planetesimals (e.g. Wyatt 2008; Krivov 2010). Besides dust, recent observations have revealed gas, mostly CO molecules, in emission in ~ 20 of these debris systems (Hughes et al. 2018). Similarly to dust particles, the detected gas is also thought to be derived from larger planetesimals and thus having a secondary origin (Kral et al. 2017), though in some very gas-rich young systems a primordial, residual origin also cannot be ruled out (Kóspál et al. 2013).

49 Cet (HD 9672) is one of the most prominent examples of young dust-rich gas-bearing debris discs. The A1V-type host star has a stellar luminosity of $16 L_{\odot}$ and an effective temperature of 9000 K (Roberge et al. 2013). Its distance is given by the new *Gaia* data release as 57.0 ± 0.3 pc (Gaia Collaboration 2016, 2018; Bailer-Jones et al. 2018). 49 Cet has been found to be a member of the 40-Myr-old Argus association (Torres et al. 2008; Zuckerman et al. 2012; Zuckerman 2019). The dust disc around 49 Cet was discovered by the *Infrared Astronomical Satellite (IRAS)* (Neugebauer et al. 1984; Sadakane & Nishida 1986) and found to be one of the brightest discs, with a fractional luminosity above 10^{-3} (Jura et al. 1993). It was first spatially resolved in the mid-infrared with the MIRLIN instrument of the Keck II 10 m telescope (e.g. Wahhaj, Koerner & Sargent 2007). However, in the mid-infrared regime the disc exhibits only a moderate amount of emission, suggesting that the dust needs to have a low temperature. 49 Cet is one of those rare gaseous debris discs where besides CO gas (Zuckerman et al. 1995) several other gas compounds have been detected either in emission (Donaldson et al. 2013; Higuchi et al. 2017) or in absorption (Roberge et al. 2014). The origin of this gas is still debated but most current evidence leans towards a second-generation origin (e.g. Hughes et al. 2017).

Recently, the results of the numerous studies of the 49 Cet debris disc were summarized in Choquet et al. (2017), who presented the first analysis of scattered light images of this disc observed by the *Hubble Space Telescope/NICMOS* and Very Large Telescope/SPHERE. The authors generated a schematic view of the system and furthermore, they investigated the possibility of existing but yet unseen planets around the 49 Cet host star. In addition to that, Hughes et al. (2017) presented ALMA images with a spatially resolved surface density distribution of the molecular gas and the dust continuum emission.

Thanks to the wide wavelength coverage of observations of 49 Cet, it is possible to compare its system properties inferred by studies at different wavelengths. An interesting question is whether we see similar disc structures for different dust grain populations. By combining near-infrared (NIR) scattered light emission, tracing smaller grains, and thermal emission in the sub-millimetre regime, sensitive to large particles, we are able to address this issue. Furthermore, by combining different kinds of observations at

multiple wavelengths, it is possible to constrain system parameters that remained unconstrained in former studies focusing on one wavelength range or type of emission. Due to developments in observational techniques and instruments this approach has become feasible for debris discs only recently, but at the time of this study a handful of analyses had addressed this topic already (e.g. Augereau et al. 2001; Ertel et al. 2011; Donaldson et al. 2013; Schüppler et al. 2015; Lobreton et al. 2016; Olofsson et al. 2016, Olofsson et al., in preparation). Never the less, most resolved discs (146, list of resolved debris discs¹; Hughes et al. 2018) do not have data in both wavelength regimes, so a detailed analysis of the disc extent in scattered light and thermal emission remains a future project.

Large dust particles are most effectively traced by observations of thermal emission at long wavelengths (e.g. far-infrared or sub-millimetre). Since these grains are not sensitive to radiation pressure forces we assume their position to be close to the planetesimal belt invisible to us. On the other hand, scattered light in the NIR is dominated by small particles that are highly affected by radiation pressure and can have highly eccentric orbits as a consequence. As a result we would expect that by observing small grains we should see a more extended dust disc than by tracing large particles at millimetre wavelengths. Indeed, for example the debris disc around β Pic shows an extent of ~ 150 au at sub-millimetre wavelengths while in NIR a halo of small particles becomes visible up to 1800 au (Ballering et al. 2016). However, for some discs such as Fomalhaut comparable disc radii are found in thermal emission and scattered light (Holland et al. 1998; Dent et al. 2000; Kalas, Graham & Clampin 2005). In the case of 49 Cet, we are fortunately able to compare former ALMA studies (Hughes et al. 2017) with observations in scattered light (this work; see also Choquet et al. 2017) to address the question of the disc extent as well. An overview of the theoretical background for the dust dynamics in debris discs is presented in Appendix A.

In this paper, we will present new *Y*-band data taken with the VLT/SPHERE and compare them to previous SPHERE *H*-band data from Choquet et al. (2017). The observations and data reduction of the SPHERE data are described in Section 2. We will analyse the radial extent of the disc at different wavelengths in Section 3. The modelling of the disc is described in Section 4. Furthermore, we will investigate the question of whether it is possible to find a model that can fit the disc parameters inferred from both thermal emission and scattered light images. Section 5 shows the analysis of the different models investigated, while the results are discussed in Section 6. A summary is given in Section 7.

2 OBSERVATIONS AND DATA REDUCTION

2.1 Broad-band SPHERE data

We observed the disc around 49 Cet in the programme 198.C–0209(N) on 2016 November 19 for 1.8 h on source with the SPHERE/IRDIS instrument of the VLT (Dohlen et al. 2008; Beuzit et al. 2019). The observations were carried out using the broad-band *Y* filter with a central wavelength of $1.04 \mu\text{m}$, a width of 139 nm, and the coronagraph N_ALC_YJ_S (Martinez et al. 2009; Carillet et al. 2011) with a diameter of 185 mas. The observations were performed in pupil tracking mode to allow for angular differential

¹<https://www.astro.uni-jena.de/index.php/theory/catalog-of-resolved-debris-disks.html>

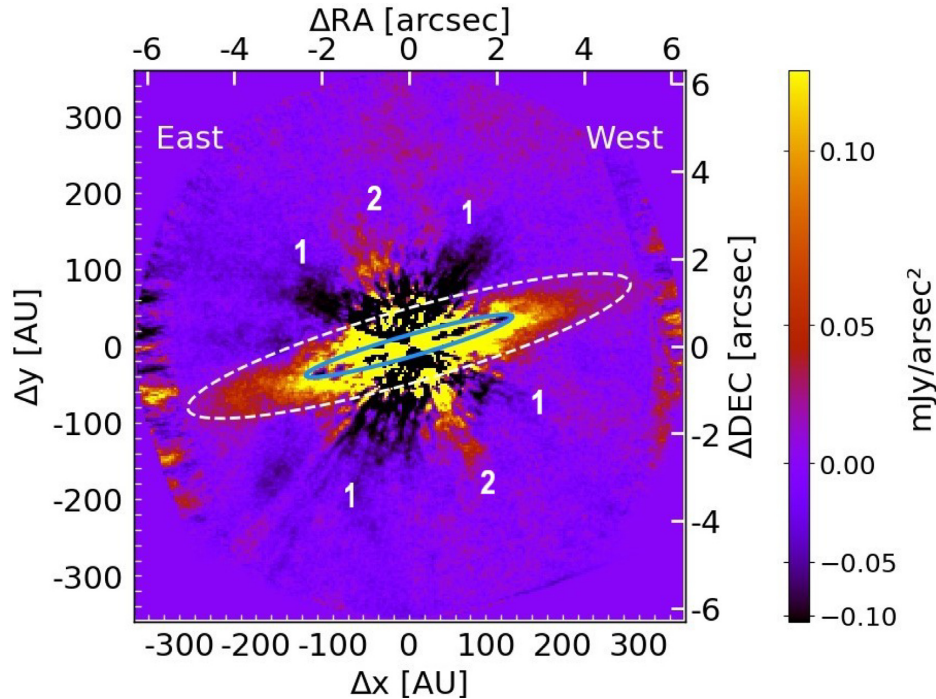


Figure 1. Classical ADI-reduced scattered light Y-band image of 49 Ceti. The white dashed line shows the inferred disc extent of 280 au, the blue solid line the location of the surface brightness peak at 140 au. The numbers 1 and 2 indicate the residuals. Further explanations are given in the text.

imaging (ADI; Marois et al. 2006). The total on-sky rotation during our observations was 70° .

After basic reduction steps (flat-fielding, bad-pixel correction, background subtraction, frame registration, frame sorting) we processed the data with a classical ADI reduction technique, which consisted of building a model point spread function (PSF) from the mean of all pupil-stabilized images, which was then subtracted from each frame before de-rotating and stacking the images.

In Fig. 1 the result of the ADI reduction of the 49 Ceti debris disc is shown. The image was normalized to mJy arcsec^{-2} in the following way. On the non-coronagraphic image, we measured the flux density encircled within a circle of radius 0.1 arcsec, encompassing the PSF core, wings, and diffraction spikes from the spiders. Then this flux density was corrected by the transmission of the neutral density filter used to obtain the non-coronagraphic image, and by the ratio between the detector integration time (DIT) of the coronagraphic and non-coronagraphic images, to obtain a reference conversion value. To convert the coronagraphic image from ADU to mJy arcsec^{-2} , the coronagraphic image was divided by the reference conversion value, multiplied by the stellar flux density found to be 11.9 Jy at the central wavelength of the Y band, and divided by the pixel surface area in arcsec^2 . The pixel scale of IRDIS is $0.01225 \text{ arcsec pixel}^{-1}$ (Maire et al. 2016). The ADI reduction algorithm induces self-subtraction of any extended astrophysical signal (Milli et al. 2012). The flux displayed in Fig. 1 did not take this self-subtraction effect into account, which requires a forward-modelling approach and is described in Section 4.3.

2.2 Narrow-band SPHERE data

We also observed 49 Ceti on 2016 July 23, with VLT/SPHERE in the framework of an open time programme 097.C-0747(A). We used pupil-stabilized imaging with the N_{ALC}-YJH_S coronagraph, having a coronagraphic mask with a diameter of 185 mas. We

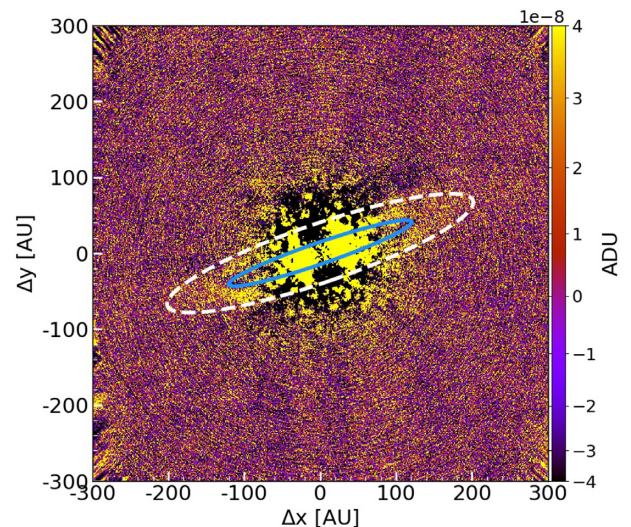


Figure 2. Classical ADI-reduced scattered light H-band image of 49 Ceti. The white dashed line shows the inferred disc extension of 200 au, the blue solid line the location of the surface brightness peak at ~ 140 au.

used the IRDIFS observing mode, which provided Integral Field Spectrograph (IFS) observations in the Y – J range and IRDIS data in the H23 dual band. The data reduction was carried out by the SPHERE Data Centre using their pipeline (Delorme et al. 2017). The obtained reduced master cubes were then utilized as input for high-contrast imaging post-processing performed by the Speckle Calibration (SPECCAL) package (Delorme et al. 2017; Galicher et al. 2018). The reduced image in ADU is depicted in Fig. 2.

3 DISC GEOMETRY AND RADIAL PROFILES

In our ADI-reduced *Y*-band image (Fig. 1) we clearly detect the debris disc of 49 Cet between a radial distance of 1.4 arcsec (80 au) and ~ 4.9 arcsec (280 au). We note that these values are detection limits and thus might not resemble the true, possibly larger, disc extent. At an angle of 45° to the semimajor axis we see dark patterns as residuals from the reduction process (shown as no. 1 in Fig. 1.). In addition to that, there seems to be emission at a 90° angle that is identified as diffraction pattern residuals stemming from the star (shown as no. 2 in Fig. 1.). In the reduced H23-band image the disc is detected between 80 and ~ 200 au where the smaller extent is caused by a weaker detection of the disc. Never the less, in contrast to the *Y*-band data, neither the dark pattern nor the diffraction spikes are visible in the H23 band.

In the following study we will focus on the *Y*-band data due to the stronger detection of the debris disc. Furthermore, we will concentrate on the resolved outer disc component and will not take a possible inner ring into account that was proposed at a location of ~ 10 au by former studies (e.g. Wahhaj et al. 2007; Chen et al. 2014; Pawellek et al. 2014).

We derived the Position Angle (PA) of the disc in the *Y* band and found a best value of $106.2^\circ \pm 1.0^\circ$. To do so, we de-rotated the disc to align the major axis with the horizontal of the de-rotator. Then we fitted the vertical profiles of the disc between a separation of 45 and 105 pixels with a Gaussian profile. We iterated with the de-rotation angle until the centroids of the Gaussian had a slope of zero (e.g. Lagrange et al. 2012; Milli et al. 2014). Comparing our PA to values from former studies that lie between 93° and 130° (see Table 1) we find a good agreement with the *Herschel*/PACS measurements. Comparing directly to other SPHERE observations is difficult since the value of 110° inferred by Choquet et al. (2017) was not fitted but fixed.

3.1 Radial profiles of scattered light images

We extracted the radial profile of the surface brightness using the method described in Choquet et al. (2017) where the authors analyse *H*-band data of 49 Cet. In this method we produce slices along the semimajor axis with a length of 93 pixels above and below the semimajor axis and a width of 2 pixels. Then we calculate the mean value of the flux density for each slice. With the sizes chosen for the slices we are able to directly compare our *Y*-band profile to the *H*-band data of Choquet et al. (2017). We estimate the noise level of the images by generating slices similar to those for the radial profile. Then we rotate these slices by 90° to get the perpendicular direction to the disc. Finally, we calculate the standard deviation of each slice.

The result is shown in Fig. 3, where we normalize the surface brightness to the flux density of the host star given as 6.4 Jy for the *H* band and 11.9 Jy for the *Y* band. Our *Y*-band observations reach a disc signal-to-noise level of 7, which is stronger than for the *H*-band data due to a longer exposure time. The noise that dominates at short separation is the residuals from the subtraction process of the PSF. Beyond ~ 3 arcsec, we are in the background-limited regime where the background noise dominates (sky background + readout noise of the detector). The noise level is in the same order of magnitude as the disc signal within a region of 80 au and thus, we will exclude the inner region from further analyses. Furthermore, the disc is detected within ~ 280 au based on the noise level as well. In case of the *H*-band data the eastern side of the disc is well detected while the western side remains close to the noise level. In

addition, the disc is found to be of a similar extent as suggested by our *Y*-band image. Analysing the radial profile, we find local peaks of the surface brightness in an area between ~ 130 and ~ 170 au in the eastern and western directions in both SPHERE images.

3.2 Radial profile of thermal emission

In order to compare the brightness profile of the NIR scattered light with the thermal dust emission in the sub-millimetre, we use ALMA data directly taken from Hughes et al. (2017), who presented 850 μm continuum images for 49 Cet with a beam size of 0.47×0.39 arcsec. To obtain the radial profile we apply the same method as described for the scattered light observations, but adapt the size of the slices according to the ALMA pixel scale of $9.765\,62\text{ mas pixel}^{-1}$. The resulting radial profile is depicted in Fig. 4. In contrast to the calculated noise level as a function of radial distance for SPHERE data we use the noise level of $0.056\text{ mJy beam}^{-1}$ as given in Hughes et al. (2017) to infer the disc radius.

We find that the eastern wing extends to ~ 280 au and the western side up to ~ 250 au, which is in agreement with the scattered light data. However, in case of the thermal emission measurements the radial profile shows a clear drop of the surface brightness around ~ 200 au down to values comparable to the noise level of $0.056\text{ mJy beam}^{-1}$, so we assume we see the real disc extent rather than a radial detection limit.

Comparing our inferred disc extent with values derived by former studies (see Table 1) we find comparable disc radii for different *Herschel*/PACS observations as well as for the SPHERE *H*-band observation.

4 MODELLING

4.1 Modelling strategy

The 49 Cet debris disc system was subject to several modelling projects, either concentrating on the dust (e.g. Wahhaj et al. 2007; Pawellek et al. 2014; Choquet et al. 2017) or the gas (e.g. Roberge et al. 2014; Miles, Roberge & Welsh 2016), or both components (e.g. Zuckerman & Song 2012; Roberge et al. 2013; Hughes et al. 2017; Nhung et al. 2017). In this study we focus on the dust component. Our goal is to investigate whether disc models inferred from thermal emission images can explain the scattered light observations obtained in the NIR.

We start with a fit of the spectral energy distribution (SED) of 49 Cet to get information on the dust grain size parameters (see Section 4.2 for a detailed description). Then we study the radial distribution of the particles. In a former study Hughes et al. (2017) investigated three different surface density profiles for the grains visible at sub-millimetre wavelengths: a single power law, a power law including a narrow dust ring, and a double-power-law model. We assume that large dust particles trace the planetesimals best and thus use the parameters of the three surface density profiles mentioned before to generate the planetesimal belts for our so-called semidynamical disc models. These models assume that dust grains are released from the planetesimals and that their orbits are altered by stellar radiation pressure. We use the term ‘semidynamical’ since no time-dependence of moving particles is taken into account. The actual profiles of the planetesimal belts from which the dust is produced are depicted in Fig. 5, while their parameters are specified in Table 2. The noise visible in Fig. 5 stems from the number of planetesimals used for the model setting. The sizes of the dust grains

Table 1. Disc parameters inferred in different wavelength ranges.

Wavelength (μm)	Radius (au)	Inclination ($^\circ$)	PA ($^\circ$)	Comments/Instrument
NIR	65–250	73	110	VLT/SPHERE, Choquet et al. (2017)
NIR	80–280	...	106 ± 1	VLT/SPHERE, this work
12.5, 17.9	30–60	60 ± 15	125 ± 10	Keck/MIRLIN, inner disc component, Wahhaj et al. (2007)
70	200	>44	105 ± 1	Herschel/PACS, Roberge et al. (2013)
70	192	67.4 ± 2.7	109.0 ± 3.9	Herschel/PACS, Moór et al. (2015)
100	196	67.2 ± 2.5	109.4 ± 4.8	Herschel/PACS, Moór et al. (2015)
160	209	56.7 ± 15.5	93.4 ± 13.9	Herschel/PACS, Moór et al. (2015)
450	421 ± 16	74 ± 13	130 ± 10	SCUBA2, Holland et al. (2017)
850	117	80.6 ± 0.4	109.1 ± 0.4	ALMA, Hughes et al. (2017)

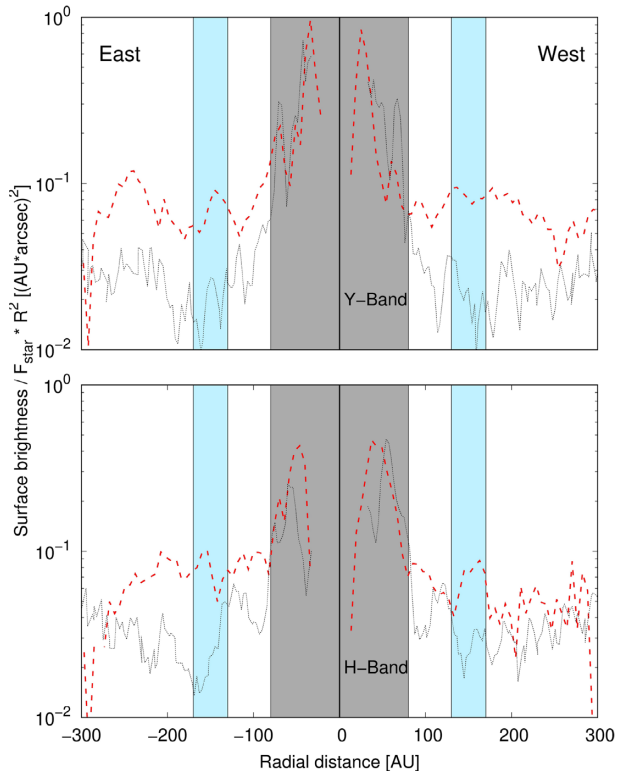


Figure 3. Surface brightness as a function of radial distance to the star for the SPHERE observations. The upper panel shows the Y-band data, the lower the H-band data. The red dashed line depicts the radial profile of the disc, the black solid line the 1σ noise level. The bright blue filled areas in both panels represent the location of symmetric peaks in the western and eastern directions. The grey filled area shows the inner region of 80 au where the noise level is comparable to the signal.

follow the distribution inferred by the SED modelling. From the semidynamical models we generate thermal emission and scattered light images. Details for this procedure are described in Section 4.3. In a final step the resulting images are compared to the observational images by forward modelling. At the time of the ALMA study (Hughes et al. 2017), the new *Gaia* distances were not available yet, so we correct the inner and outer disc radii for them.

4.2 SED modelling

The photometric data are collected from the literature and summarized in Table 3. We use the SONATA code (Pawellek et al. 2014; Pawellek & Krivov 2015) to fit the SED and apply the same stellar photospheric model used in Pawellek et al. (2014) to

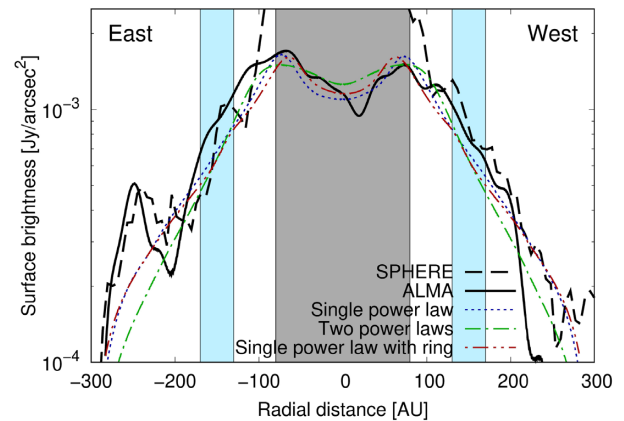


Figure 4. Surface brightness as a function of radial distance. The thick black solid line shows the observational data for ALMA, the black dashed line for the SPHERE H band normalized to the ALMA data. The blue dotted line shows the disc with a single-power-law radial profile, the green dash-dotted line a two power-law radial profile, and the red dash-dotted line a single power law including a narrow dust ring. The blue shaded areas represent symmetric peaks in western and eastern directions at the same position as in Fig. 3. The grey filled area shows the inner region of 80 au.

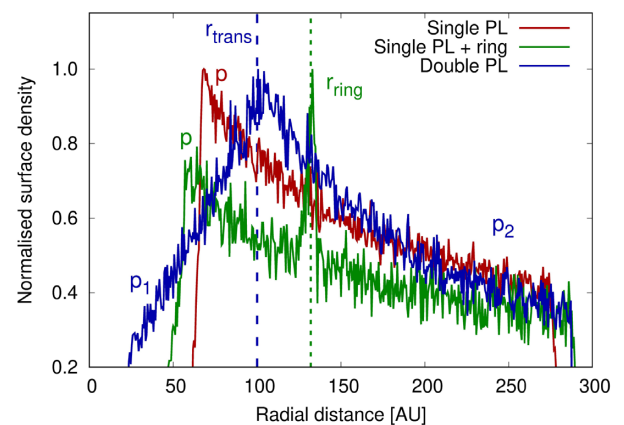


Figure 5. Surface density profiles for the parent belts inferred from semidynamical models. Red shows the single power law, green the power law including a narrow ring, and blue the double-power-law model. The vertical green dotted line and the blue dashed line give the positions of the planetesimal ring and the transition radius, respectively. The different radial distribution indices used for the models are depicted at the corresponding parts of the profiles. The noise is caused by the finite number of planetesimals in the models.

Table 2. Parameters for the radial distribution models.

Parameter		Single power law				Double power law	
		No ring		With ring		H17	Fit
		H17	Fit	H17	Fit	H17	Fit
	i (°)	79.3		79.3		79.2	
	PA (°)	108.7		108.8		108.3	
	r_{\min} (au)	70		58		26	
	r_{\max} (au)	298		291		302	
p	Range	...	0.0–2.0	...	0.0–1.5
	Step size	...	0.2	...	0.5
	Value	1.27	0.6	0.75	0.5
r_{ring} (au)	Range	90–150
	Step size	10
	Value	...		109	140
r_{trans} (au)	Range	50–170
	Step size	20
	Value		92	110
p_1	Range	–3.0–0.0
	Step size	0.5
	Value		–2.7	–1.0
p_2	Range	0.0–2.0
	Step size	0.5
	Value		1.50	1.0
χ_{red}^2	Thermal	1.40	1.18	1.30	1.16	1.32	1.15
	Scattered	2.38	2.11	2.37	2.16	2.37	1.99

Notes. The parameter values of the first table part were taken from Hughes et al. (2017), corrected for the new distance of 57.1 pc, and used for the modelling of this work. In the second part of the table the values in column ‘H17’ stem from Hughes et al. (2017) and are corrected for the new distance of 57.1 pc. Parameters in the column ‘Fit’ are the best-fitting results of this work.

determine the influence of the host star. Here, the stellar temperature, metallicity, and surface gravity are taken into account to generate a synthetic spectrum by interpolating the PHOENIX-GAIA model grid (Brott & Hauschildt 2005). The dust composition is assumed to be astronomical silicate (Draine 2003) with a bulk density of 3.3 g cm^{-3} .

The SONATA code calculates the temperature and the thermal emission of each dust particle at a given distance to the star, where the number of particles is determined by the dust mass. Then it sums up the emission of all particles to generate the SED. The flux densities given for wavelengths shorter than $10 \mu\text{m}$ are not used to fit the dust disc since in this wavelength regime the stellar photosphere rather than the dust dominates the emission. The code assumes a power law for both the radial and the size distribution of the dust using the surface number density $N(r, s)$:

$$N(r, s) \sim \left(\frac{r}{r_0}\right)^{-p} \times \left(\frac{s}{s_0}\right)^{-q}. \quad (1)$$

Here, r represents the disc radius, s the grain radius, s_0 and r_0 normalization factors, and p and q the power-law indices for the radial and size distribution. The surface number density is directly connected to the surface density, $\Sigma(r, s)$, by

$$\Sigma(r, s) ds = \pi s^2 \times N(r, s) ds. \quad (2)$$

Due to the fact that SEDs use photometric data integrated over the whole disc area, they cannot differentiate between different radial profiles. Therefore, we assume the same single-power-law model given by Hughes et al. (2017) with $p = 1.27$, $r_{\min} = 70 \text{ au}$, and $r_{\max} = 298 \text{ au}$ to fit the SED.

We assume the grain sizes lie between a minimum and a maximum value, s_{\min} and s_{\max} . We fix the maximum grain size to 1 cm , because larger grains do not contribute any more to the

SED in the wavelength range observed. Furthermore, we fix the radial parameters and hence, we are left with three free parameters to fit, namely the minimum grain size, s_{\min} , the size distribution index, q , and the amount of dust, M_{dust} , for particles between s_{\min} and s_{\max} . We infer the amount of dust by using the bulk density ϱ and the dust volume V :

$$M_{\text{dust}} = \varrho \times V = \varrho \times \frac{4\pi}{3} \int_{s_{\min}}^{s_{\max}} 2\pi \int_{r_{\min}}^{r_{\max}} N(r, s) r dr s^3 ds. \quad (3)$$

Roughly two-thirds of all discs investigated so far show evidence for an asteroid belt analogue (also called the warm component) in addition to an Edgeworth–Kuiper belt analogue (cold component; e.g. Ballering et al. 2013; Chen et al. 2014; Pawellek et al. 2014). We apply the criteria given in Pawellek et al. (2014) to check for the presence of a warm component for 49 Cet and indeed, our modelling results suggest the existence of an inner dust belt as well. Since there is a large degeneracy between the outer and inner disc parameters, we have to make several assumptions for our SED model. At first we have to identify the location of the warm component, which is not spatially resolved in the images. To do so, we fit the warm dust component with a pure blackbody model to infer its blackbody radius. Here we assume the same radial distribution index ($p = 1.27$) as for the outer component. The blackbody radius is found to be $\sim 8 \text{ au}$. Now, we estimate the ‘true’ disc radius by applying the method presented in Pawellek & Krivov (2015) and Pawellek (2017). Here the authors found a relation between the true disc radius and the blackbody radius in the shape of

$$\frac{R_{\text{disc}}}{R_{\text{blackbody}}} = A \times \left(\frac{L}{L_{\text{sun}}}\right)^B. \quad (4)$$

For pure astronomical silicate Pawellek (2017) gives the parameters as $A = 6.49 \pm 0.86$ and $B = -0.37 \pm 0.05$. Using these values

Table 3. Continuum flux density.

Wavelength (μm)	Flux density (mJy)	Instrument	Reference
0.44	$22\,260 \pm 350$	<i>TYCHO</i>	1
0.55	$21\,600 \pm 200$	<i>TYCHO</i>	1
1.24	$10\,180 \pm 190$	2MASS	2
1.65	6300 ± 130	2MASS	2
2.16	4373 ± 81	2MASS	2
3.35	1990 ± 120	<i>WISE</i>	3
4.60	1294 ± 49	<i>WISE</i>	3
5.86	690 ± 70	IRS	4
7.07	480 ± 50	IRS	4
8.97	320 ± 30	IRS	4
9.0	366 ± 13.5	<i>AKARI/IRC</i>	5
10.8	250 ± 50	Keck/MIRLIN	6
11.40	210 ± 20	IRS	4
11.56	211 ± 21	<i>WISE</i>	3
12.0	330 ± 66	<i>IRAS</i>	6
12.50	200 ± 26	Keck/MIRLIN	8
13.90	180 ± 20	IRS	4
17.90	186 ± 25	Keck/MIRLIN	8
18.0	199 ± 16	<i>AKARI/IRC</i>	5
22.09	238 ± 24	<i>WISE</i>	3
24.00	259 ± 10	<i>Spitzer/MIPS</i>	9
25.0	380 ± 76	<i>IRAS</i>	7
60.0	2000 ± 400	<i>IRAS</i>	7
63.19	2090 ± 350	<i>Herschel/PACS Spec</i>	9
70.00	2163 ± 151	<i>Herschel/PACS</i>	10
71.42	1749 ± 123	<i>Spitzer/MIPS</i>	10
72.84	1950 ± 320	<i>Herschel/PACS Spec</i>	9
78.74	1900 ± 310	<i>Herschel/PACS Spec</i>	9
90.0	1776 ± 295	<i>AKARI/FIS</i>	5
90.16	1880 ± 320	<i>Herschel/PACS Spec</i>	9
100.0	1910 ± 380	<i>IRAS</i>	7
100.0	1919 ± 134	<i>Herschel/PACS</i>	10
145.54	1160 ± 180	<i>Herschel/PACS Spec</i>	9
150	750 ± 500	ISO	4,11
157.68	980 ± 130	<i>Herschel/PACS Spec</i>	9
160.00	1066 ± 75	<i>Herschel/PACS</i>	10
170	1100 ± 500	ISO	4,11
250.00	372 ± 27	<i>Herschel/SPIRE</i>	9
350.00	180 ± 14	<i>Herschel/SPIRE</i>	9
450.0	125 ± 18	JCMT/SCUBA-2	12
500.00	86 ± 9	<i>Herschel/SPIRE</i>	9
850.0	17 ± 3	ALMA	4
850.00	13.5 ± 1.5	JCMT/SCUBA-2	12
1200.00	12.7 ± 2.8	IRAM	13
1300.0	2.1 ± 0.7	CARMA	4
1330	5.5 ± 0.7	ALMA/ACA	14
9000.0	0.0251 ± 0.0055	VLA	15

Note. References: [1] – Høg et al. (2000); [2] – 2MASS All-Sky Catalog of Point Sources; [3] – Wright et al. (2010); [4] – Hughes et al. (2017); [5] – AKARI All-Sky Survey Bright Source Catalog; [6] – Jayawardhana et al. (2001); [7] – *IRAS* Faint Source Catalog; [8] – Wahhaj et al. (2007); [9] – Roberge et al. (2013); [10] – Moór et al. (2015); [11] – ISO; [12] – Holland et al. (2017); [13] – Bockelée-Morvan et al. (1994); [14] – Moór et al. (in preparation); [15] – MacGregor et al. (2016).

and the solar luminosity of $16 L_{\odot}$, we find an estimated ‘true’ location of the warm component of ~ 16 au. We assume the same minimum grain size and size distribution index for both the warm and cold components and therefore increase the number of free parameters from three to four by adding the amount of dust of the warm component. The SONATA code uses the simulated annealing approach (Pawellek et al. 2014) to fit the SED. Considering the

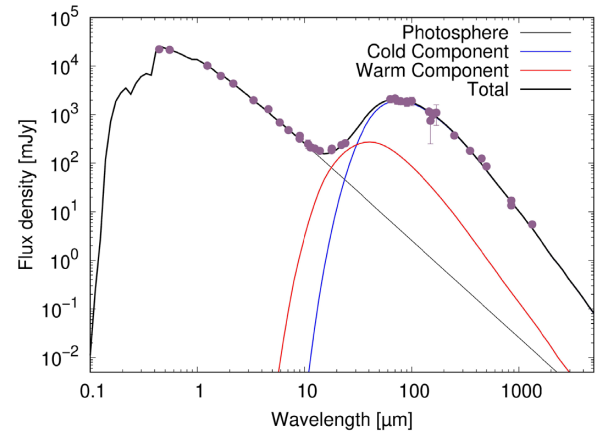


Figure 6. The SED of 49 Ceti using pure astronomical silicate with a bulk density of 3.3 g cm^{-3} for the outer and inner component. The thin black solid line represents the stellar photosphere, the red solid line shows the warm inner ring, and the blue lines show the outer belt.

Table 4. Parameters for the grain size distribution assuming a single-power-law radial profile.

Parameter	Best-fitting values	Comment
s_{min} (μm)	5.14 ± 0.76	...
s_{max} (μm)	10 000	Thermal emission, fixed
	15	Scattered light, fixed
q	3.77 ± 0.05	...
f_d	8.8×10^{-4}	...
T_{dust} (K)	65 ± 3	...
T_{warm} (K)	125 ± 2	...
χ^2_{red}	1.03	...

Notes. The blow out limit is given for pure astronomical silicate as $2.9 \mu\text{m}$. The different maximum grain sizes are explained in Section 4.3. For the dust temperature of both components we take the wavelength of the SED peak and calculate the temperature by using Wien’s displacement law.

scattered light images, we are not sensitive to the region within 80 au. Thus, we focus on the cold dust component of the debris disc.

In the best-fitting SED model the minimum grain size is $s_{\text{min}} = 5.14 \pm 0.76 \mu\text{m}$ and the size distribution index $q = 3.77 \pm 0.05$. These parameters are applied to all semidynamical models with the different radial profiles analysed in this work. We checked the validity of our assumption by using the double power law as radial profile for the SED (Table 2) and found the grain size parameters to be close to the values of the single-power-law model lying within their given confidence intervals. The resulting SED is shown in Fig. 6 while the grain size parameters are given in Table 4. The amount of dust, M_{dust} , in debris discs depends on the SED model settings, i.e. the grain size and radial distribution, and is therefore difficult to compare for different studies. Hence, we focus on the fractional luminosity, which is only determined by photometric data points. It is given as $f_d = 8.8 \times 10^{-4}$.

The error bars give the uncertainties of the fit parameters and are inferred in the following way. We start from the position of the minimum χ^2 in the parameter space. New parameter values are generated and the resulting χ^2 of the model is compared to its minimum value. There is a probability that a new minimum can be found in the direction of the new parameter values. If this probability

reaches a critical value, then the fit parameters are saved. In the end, it is counted how often the code reaches a certain parameter value. The resulting distribution in the parameter space represents an estimate for the probability distribution of the parameters and thus allows us to calculate the confidence levels for the parameters assuming that the values follow a normal distribution (simulated annealing; e.g. Pawellek 2017).

4.3 Generating images

After fitting the SED we generate the semidynamical disc models using the MODERATO code (Olofsson et al., in preparation; for similar approaches see Wyatt et al. 1999; Lee & Chiang 2016). The code assumes surface density profiles for the parent belt where each planetesimal releases grains of different sizes following a power law (see equation 1). Then the orbits of the individual dust particles altered by stellar radiation pressure are calculated and from their position the scattered light and thermal emission are inferred. We correct for the possible overabundance of highly eccentric small particles in the way described by Strubbe & Chiang (2006) and Thébaud & Wu (2008).

The radial and grain size distributions assumed for the models are given in Tables 2 and 4. For each radial profile a small grid of parameter values is assumed to find the best-fitting model. Due to the high calculation time for one run, Monte Carlo fitting is not applicable. In all cases we fix the inclination, PA, and minimum and maximum disc radii to the values inferred by Hughes et al. (2017) to generate the thermal emission maps. Considering the scattered light maps we use the PA of 106.2 inferred in this work.

In the first scattered light study of 49 Cet, Choquet et al. (2017) use the anisotropic scattering approach by Henyey & Greenstein (1941) where a single scattering asymmetry factor, $|g|$, is assumed for the whole material without differentiation between grain sizes. In scattered light studies of debris discs, this approach is often used to get a general idea of the scattering properties of the disc material (e.g. Schneider et al. 2006; Thalmann et al. 2013; Millar-Blanchaer et al. 2015; Olofsson et al. 2016; Engler et al. 2018). Since we generate a physical model with a distribution of particles inferred by SED fitting, we use Mie theory instead to stay consistent and assume pure astronomical silicate (Draine 2003) as the dust composition, similarly to the SED modelling. However, we additionally use the Henyey–Greenstein (HG) approach to compare our results to previous studies.

We are aware that using Mie theory to calculate the optical properties for scattered light models leads to an overestimation of forward scattering, especially for larger particles ($\geq 20 \mu\text{m}$) since the grains are assumed to be compact spheres (e.g. Schuerman et al. 1981; Bohren & Huffman 1983; Weiss-Wrana 1983; Mugnai & Wiscombe 1986; McGuire & Hapke 1995).

To avoid this effect we assess the maximum grain size still contributing to the scattered light. This is done by estimating the width of the forward scattering peak. The minimum scattering angle achievable for a disc is given by the disc inclination:

$$\alpha = 90^\circ - i, \quad (5)$$

which is $\approx 10^\circ$ in the case of 49 Cet. On the other hand, analogously to a telescope, a dust particle of radius s can ‘detect’ incoming light (Babinet’s principle) with a geometric area πs^2 and therefore, the Rayleigh criterion provides the minimum angle observable for the grain at a certain wavelength λ :

$$\alpha = 1.22 \times \frac{\lambda}{2 \times s} = 70^\circ \times \frac{\lambda}{2 \times s}. \quad (6)$$

Equalizing the angles of equations (5) and (6), it is possible to infer a grain radius for which the scattered light observations are still sensitive. We get an estimate for the maximum particle size of the 49 Cet debris disc as

$$s \approx \frac{\lambda \times 70^\circ}{2 \times (90^\circ - i)} = \frac{1.04 \mu\text{m} \times 70^\circ}{2 \times 10^\circ} = 3.5 \mu\text{m}. \quad (7)$$

This shows that the scattered light contribution of particles larger than $3.5 \mu\text{m}$ is minor, which is in agreement with Zubko (2013). In this study, the authors analysed the contribution of large particles in cometary dust by using the discrete dipole approximation method. They found that for a dust composition with moderate or high absorption, such as carbonaceous material, grains with a size parameter $x = 2\pi \times s/\lambda > 15$ are not needed to model the scattered light observations. However, adding large grains to the model did not change the results significantly, although the computation time was much higher.

With SED fitting we found a minimum grain size of $\sim 5 \mu\text{m}$, which is not contradictory to the above-mentioned estimate. It just states that the larger particles are not as effectively traced as smaller grains. Due to possible estimation uncertainties we set the maximum particle size for scattered light observations to a value of $15 \mu\text{m}$.

The semidynamical models are compared to scattered light observations by subtracting the convolved disc model from our pupil-stabilized cube of frames. Then we perform ADI on this cube to get the final image. In case of thermal emission, the models are convolved with the assumed ALMA beam and then subtracted from the observational image. We use a scaling factor to adapt the flux density of the model to our observations for scattered light and thermal emission. This is inevitable since calculating the flux density of all dust particles necessary to equal the measured emission exceeds the computational resources available. Due to the different subtraction processes we note that the scaling factors are different for scattered light and thermal emission. To estimate the quality of the model matching the observations we use χ^2 minimization assuming that an ideal residual image should expose no emission in any pixel. The χ^2 parameter is then computed for each pixel by

$$\chi^2 = \sum_{i=1}^{N_{\text{pixel}}} \left(\frac{F_i}{F_{\text{noise}}} \right)^2. \quad (8)$$

In case of the scattered light data, the noise (or error) is estimated in the following way. We use the noise level inferred from the observational image (see Fig. 3). Then we rotate this profile around the centre of the image to generate a noise map. In case of the thermal emission image we use the noise level given as $F_{\text{noise}} = 0.056 \text{ mJy beam}^{-1}$ (Hughes et al. 2017). The number of pixels for the thermal emission maps is 1024×1024 and for the scattered light images 255×255 .

5 ANALYSIS

5.1 Thermal emission

The thermal emission image observed by Hughes et al. (2017) with ALMA at $850 \mu\text{m}$ is compared to the semidynamical models based on the three different radial profiles given in Table 2 and illustrated in Fig. 5. The best-fitting results are shown in Figs 7–9.

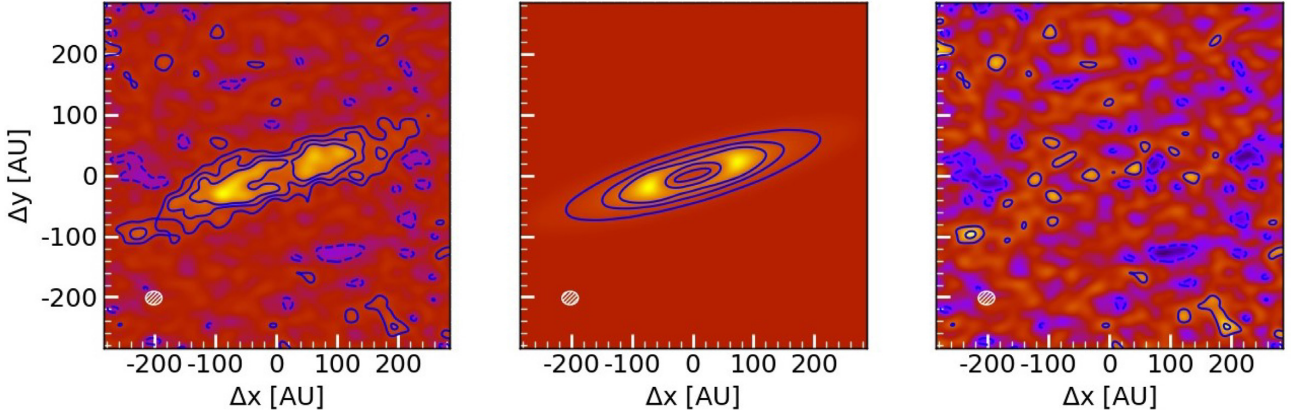


Figure 7. Modelling results of 49 Ceti. Left: ALMA image at 850 μm . Middle: best-fitting model using a single-power-law radial distribution with $p = 0.6$ generated with MODERATO. A grain size distribution with $s_{\text{min}} = 5.14 \mu\text{m}$, $s_{\text{max}} = 1.00 \text{cm}$, and $q = 3.77$ was used to generate the disc. Right: subtraction of the model disc from the observational data. The contour levels show 2, 4 and 6 times the σ level given as $0.056 \text{mJy beam}^{-1}$ in Hughes et al. (2017). The dotted contours give the negative scale, the white dashed area the beam size. The data are normalized to their maximum. The value of χ_{red}^2 is 1.18.

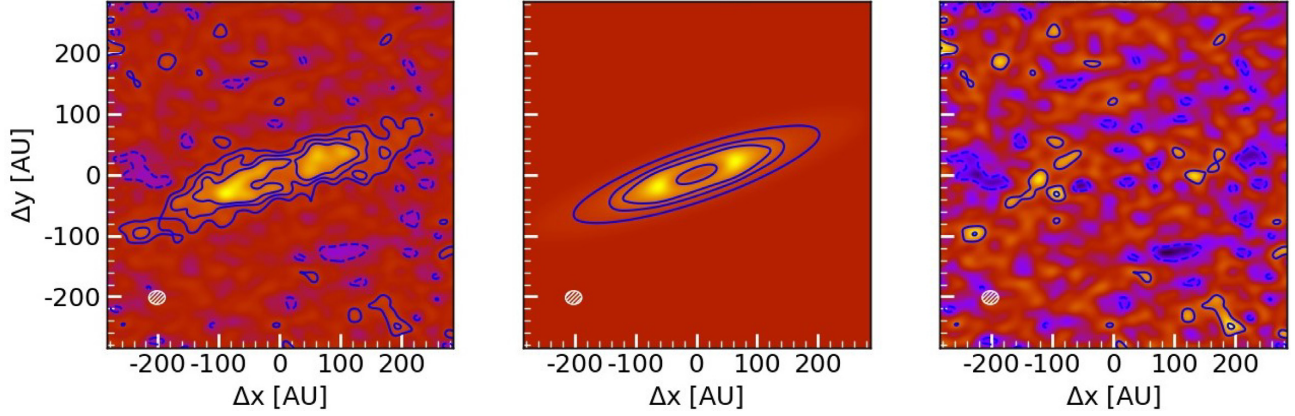


Figure 8. Same as Fig. 7, but now using the single-power-law radial distribution with $p = 0.5$ including an additional narrow ring at $r_{\text{ring}} = 140 \text{au}$. For this model $\chi_{\text{red}}^2 = 1.16$.

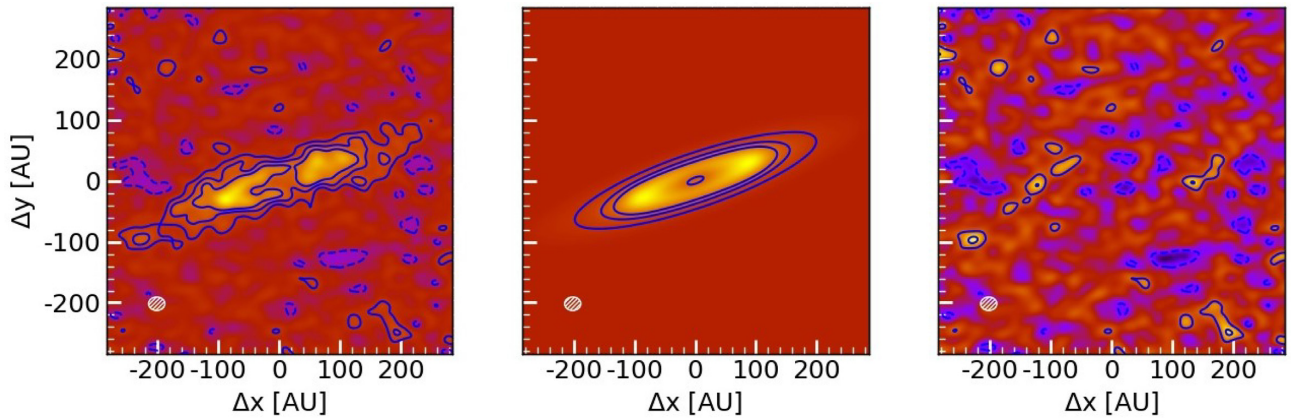


Figure 9. Same as Fig. 7, but now using the double-power-law radial profile with a transition radius of $r_{\text{trans}} = 130 \text{au}$ and radial distribution indices of $p_1 = -1.0$ and $p_2 = 1.0$. The best-fitting χ_{red}^2 is 1.15.

5.1.1 Single-power-law distribution

At first a single-power-law model is assumed as the radial distribution. Using the parameter values from Hughes et al. (2017), where the disc is confined between 70 and 298 au and possesses a surface density power law exponent of 1.27, we get a reduced χ^2 of $\chi_{\text{red}}^2 = 1.4$.

The grain parameters derived by SED fitting are applied to our model, where the minimum grain size is 5.14 μm , the maximum grain size is 1.0 cm, and the distribution index $q = 3.77$.

Next, we analyse a small parameter grid. Here, we fix the minimum and maximum disc radii as well as the inclination and PA, while only one parameter, p , is varied between 0.0 and 2.0 in steps of 0.2. The result of this fit is shown in Fig. 7, where $p = 0.6$ is the best-fitting value. We could achieve $\chi_{\text{red}}^2 = 1.18$. After subtracting the model from the observed data, there are some 2σ residual structures left throughout the disc. However, they do not seem to be of a systematic origin.

5.1.2 Single-power-law distribution with a narrow ring

In a second approach a narrow dust ring is added to the single power law of the radial distribution. The parameter values can be found in Table 2. Here, $N(r, s)$ of the extended disc is calculated at the location of the ring. Then the surface number density of the ring is set to a value twice as high, which is in agreement with the parameters given by Hughes et al. (2017). In the final step, the grains of both model parts (disc + ring) are summed up to derive the thermal emission map.

The parameters given by Hughes et al. (2017) lead to $\chi_{\text{red}}^2 = 1.30$, which is an improvement to their pure single-power-law model. The ring is confined between 108 and 110 au and possesses the same grain size parameter values as the extended disc between 58 and 291 au.

Fitting a grid of models, we vary two parameters: the distribution index p between 0.0 and 1.5 in steps of 0.5 and the position of the included ring (r_{ring}) between 90 and 150 au in steps of 10 au. The results are shown in Fig. 8, where we found a best-fitting model with $p = 0.5$ and a ring position of $r_{\text{ring}} = 140$ au. The parameter χ_{red}^2 is 1.16 and thus, slightly smaller than for the pure single-power-law model. Analysing the residual image (right-hand panel) there are less residuals found in the inner part of the disc in contrast to the single-power-law model while in the outer region some larger residuals are left.

5.1.3 Double-power-law distribution

The third approach contains a double-power-law distribution as the radial profile. To implement this setting, a similar approach to that for the former model is used. We calculate $N(r, s)$ at the position of the transition radius, r_{trans} . At this position, one power law changes into the other. We demand that $N(r, s)$ has to be the same value for both parts of the radial profile to ensure a continuous surface density profile.

Hughes et al. (2017) inferred a transition radius between both profile parts at 92 au while the inner disc region is given with $p_1 = -2.7$ and the outer fixed to $p_2 = 1.5$. Using these values we get a χ_{red}^2 of 1.32.

Now we vary the transition radius between 50 and 170 au in steps of 20 au and the radial distribution indices between -3.0 and 0.0 for the inner disc region and 0.0 and 2.0 for the outer one in steps of 0.5 each, leading to three free parameters. The best-fitting model yields

$r_{\text{trans}} = 110$ au, $p_1 = -1.0$, and $p_2 = 1.0$ and leads to $\chi_{\text{red}}^2 = 1.15$. The result is depicted in Fig. 9. Comparable to the single-power-law model including a narrow ring the inner disc region shows no systematic residuals, while in the outer part some 2σ remnants are left.

5.1.4 Comparing the models

By comparing the different radial profiles we find that all models achieve a similar χ_{red}^2 value between 1.15 and 1.18. Thus, a conclusion of which model gives the best result is hardly possible. Therefore, we apply the Bayesian information criterion (BIC), being defined as

$$\text{BIC} = \chi^2 + J \times \log_e(N), \quad (9)$$

where J gives the number of free parameters and N the number of data points. The resulting values for each model are given in Table 5.

Following the classification given in Kass & Raftery (1995), we compare each model by calculating the parameter $B = 2\log_e(\Delta\text{BIC})$, where ΔBIC represents the difference of BIC between the models. If B lies between 0 and 2, the more complex model is not significantly better than the simple model, if it lies between 2 and 6 it is possible that the more complex model is better, and if it lies between 6 and 10 the more complex model is more likely. For values larger than 10 the probability of the more complex model is much higher than for the simple one.

We now compare the models 2 and 3 (see Table 5) with the single-power-law model. Model 2 reaches a value of $B = 19.9$, while model 3 gives $B = 20.1$. This indicates that the single-power-law model including a ring and the double-power-law model have a much higher probability than the single-power-law model. In the final step we compare model 2 with model 3 and find $B = 18.5$. Thus, although the difference in χ_{red}^2 is only minor, the information criterion clearly states that the double-power-law model is preferable to the power-law model including a narrow ring.

Our fitting results deliver slightly different values than provided by the model of Hughes et al. (2017). The main difference here is that in the aforementioned study the applied surface density models for the dust grains do not consider a grain size distribution or any forces altering the particle orbits. We assume a dust orbital model including radiation pressure and a particle size distribution to generate thermal emission maps. Never the less, both approaches show that a single-power-law distribution might not be the appropriate way to simulate the debris disc of 49 Cet.

5.2 Scattered light

In this section the best-fitting models inferred from the ALMA data are compared to the scattered light data presented in this work. For reasons of comparability we also analyse the models with parameters stemming from Hughes et al. (2017). We use the grain size values given in Table 4 and the radial parameters listed in Table 2. The results are shown in Figs 10–12.

The surface density distribution of each planetesimal belt is calculated in the same way as for the thermal emission maps. Each planetesimal then releases dust particles which are influenced by radiation pressure. From the position of the grain the appropriate scattered light is derived and summed up into a map. In contrast to the thermal emission images the scattered light maps possess a complex artefact structure inclined by 45° and 90° to the major axis, which makes the interpretation of the modelling results difficult. So

Table 5. Comparison of thermal emission models.

No.	Model	J	Free parameters	$\chi^2 (\times 10^6)$	BIC ($\times 10^6$)
1	SPL	2	Scaling, p	1.24	1.24
2	SPL+ring	3	Scaling, p , r_{ring}	1.22	1.22
3	DPL	4	Scaling, p_1 , p_2 , r_{trans}	1.21	1.21

Notes. SPL is the single-power-law model, SPL + ring the single power law including a narrow ring, and DPL the double-power-law model. The number of data points assumed is the number of pixels: $N = 1024 \times 1024$.

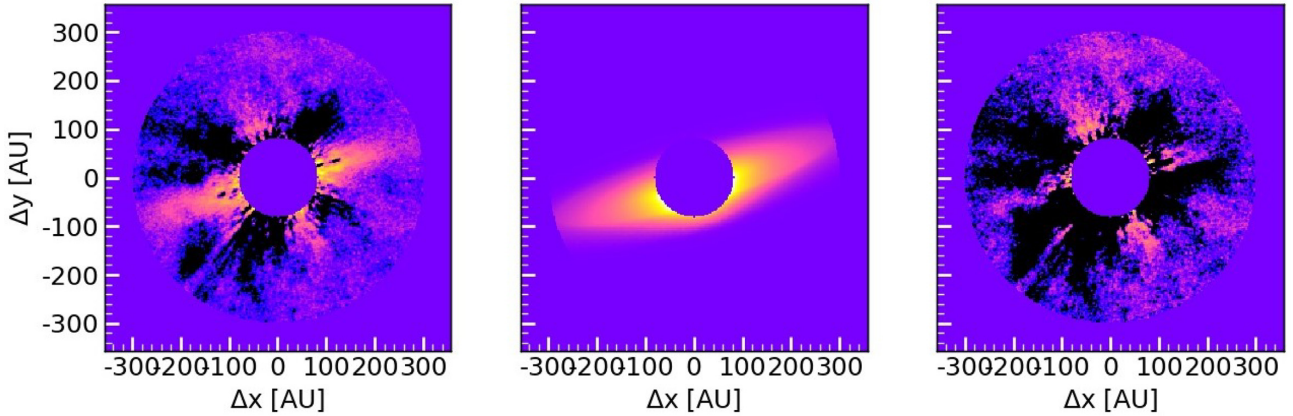


Figure 10. Modelling results of 49 Ceti. Left: ADI-reduced Y-band image as shown in Fig. 1 excluding the region within 80 au. Middle: model generated with MODERATO assuming a single power law as radial distribution with $p = 0.6$. Right: subtraction of the model disc from the observational data. The model leads to $\chi_{\text{red}}^2 = 2.11$.

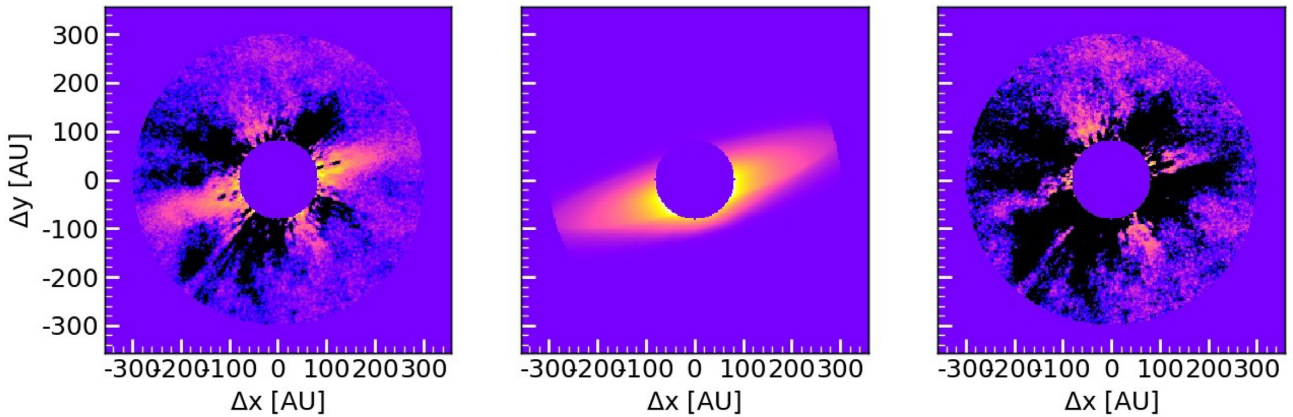


Figure 11. Same as Fig. 10, but now using the single-power-law radial distribution with $p = 0.5$ including an additional narrow ring at $r_{\text{ring}} = 140$ au. For this model $\chi_{\text{red}}^2 = 2.16$.

far there is no criterion to distinguish the artefact areas from the actual scattered light, so we cannot exclude these parts from χ^2 calculations.

Never the less, we find that all three surface density profiles can describe the scattered light observations to a certain extent, but we see residuals along the major axis and oversubtraction in the inner region close to the central star for all three radial profiles. However, the residuals in the outer disc region are of the same order as the estimated noise level of the image.

Due to the artefact structures in the image in combination with the method to find the best fit (see equation 8), the χ^2 values inferred by forward modelling are very large and thus, we again use the BIC introduced in the former section to compare the models with each other. The results are listed in Table 6.

By following the classification of Kass & Raftery (1995) again, we find that the probability of a double-power-law profile is higher than the single power law and the power law including a narrow ring. Hence, the scattered light data lead to similar results as the thermal emission data showing that a double-power-law profile as depicted in Fig. 5 is more likely to occur in the debris disc around 49 Ceti than the other profiles investigated in this study.

6 DISCUSSION

6.1 Radial profiles

We found that the radial extent of the 49 Ceti debris disc is the same for both ALMA and SPHERE observations as shown in Fig. 4. As

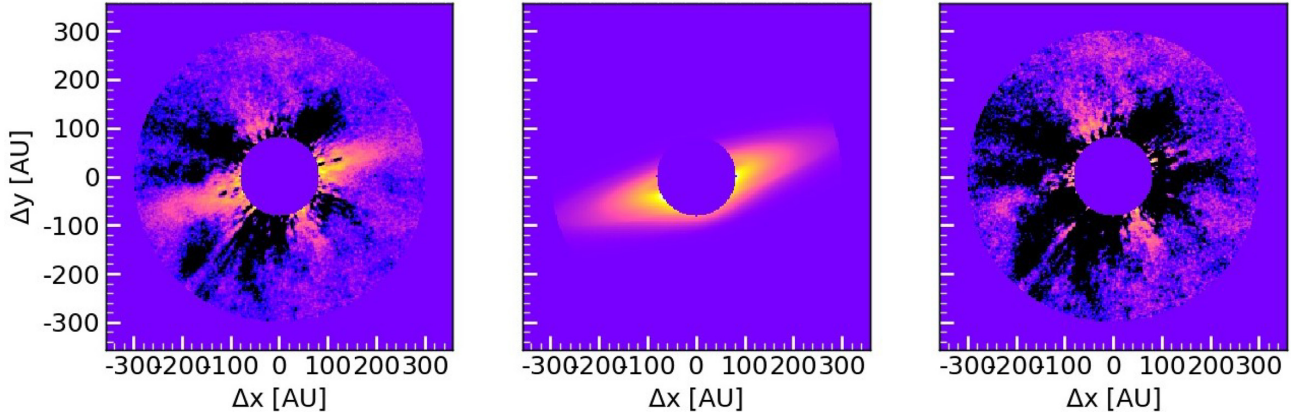


Figure 12. Same as Fig. 10, but now using the double-power-law radial profile with a transition radius at $r_{\text{trans}} = 130$ au and radial distribution indices of $p_1 = -1.0$ and $p_2 = 1.0$. The best-fitting χ^2_{red} is 1.99.

Table 6. Comparison of scattered light models.

Comparing models	$\chi^2 (\times 10^9)$	B
1, 2	8.58	4.8
1, 3	8.58	6.2
2, 3	8.58	4.8

Notes. The model numbers are given in Table 5. The number of data points assumed is the number of pixels of the scattered light image: $N = 255 \times 255$.

theory predicts, the orbits of small grains should be highly altered by radiation pressure and thus, we would expect a larger disc extent for our scattered light image than for the thermal emission map. A reason could be the rather noisy scattered light detection of the disc only showing the brightest parts of it, so we underestimate its outer radius in scattered light.

In comparison to other disc detections with SPHERE (e.g. Olofsson et al. 2016; Wahhaj et al. 2016; Engler et al. 2018) the disc of 49 Ceta, while possessing a large fractional luminosity, is rather faint in its surface brightness. On one hand this might indicate a dust composition that is strongly absorbing, such as carbon. On the other hand it might indicate the absence of small dust particles, which is supported by the results of the SED fit and other studies focusing on thermal emission and reporting that the disc is faint even in the mid-infrared (Wahhaj et al. 2007). Another explanation is that the disc possesses a broad extent from at least 80 au up to 280 au (see Fig. 3). Thus, a high number of small dust grains might be present in the disc, but due to its large on-sky area the particles are widely distributed, so the surface brightness stays low. In addition to that, the ADI reduction process (Marois et al. 2006) leads to a stronger subtraction for broad discs and so the low detection might be an observational bias.

While the single-power-law profile was already excluded as the best-fitting model by the aforementioned ALMA study (Hughes et al. 2017), the power law including a ring and the double-power-law profile remained indistinguishable for the analysis of thermal emission. To a certain extent we could reproduce this result with our semidynamical models, but we found that all three profiles are capable of describing the observational data (Fig. 4). Nevertheless, we found different parameter values for the best-fitting fiducial discs. Applying the Bayesian information criterion, we found that

despite the comparable χ^2 values for all three profiles, the double power law has the highest probability.

Summarizing the results, we infer the following architecture of the outer region of the debris disc around 49 Ceta. From observed surface brightness profiles we find that the Kuiper belt analogue is located between 80 and 280 au and shows an increase of small particles between 130 and 170 au visible in scattered light (Fig. 3). Assuming the best-fitting double-power-law model, a maximum for large grains, seen at sub-millimetre wavelengths, is found around 110 au. The edges inwards and outwards of the ring are shallow.

6.2 Size distribution

Pawellek et al. (2014) found a weak relation between the minimum grain size and the stellar luminosity of the host star. However, they stated that this trend is also consistent with being independent of the stellar luminosity and found an average value of roughly $5 \mu\text{m}$ to be valid for the majority of debris discs investigated. This is in good agreement with our SED-fit results where a value of $5.14 \pm 0.76 \mu\text{m}$ was found as the dominant grain radius. The ratio of the minimum particle size to the inferred blow-out limit of $2.9 \mu\text{m}$ for astrosilicate is 1.7. While it is directly connected to the dynamical excitation of dust-producing planetesimals in the disc, the low value of the ratio argues for a collisionally active disc for which a value around 2 is suggested (e.g. Krivov, Löhne & Sremčević 2006; Thébault & Augereau 2007).

As shown in former studies (e.g. Pawellek 2017), the size distribution index, q , is mostly influencing the steepness of the SED longwards of the far-infrared wavelengths. Hence, the now available VLA data at 9 mm (MacGregor et al. 2016) help to strengthen the constraint. Compared to an idealized collisional cascade, where the index lies at $q = 3.5$ (Dohnanyi 1969), we inferred a value of 3.77 ± 0.05 . This is somewhat larger, but still in agreement with collisional models (e.g. Löhne, Krivov & Rodmann 2008; Gáspár et al. 2012; Kral, Thébault & Charoz 2013; Löhne et al. 2017). The result supports the assumption of a dynamically excited disc producing more grains closer to the blow-out limit.

Besides a higher excitation level, which is expected for discs around earlier-type stars (Pawellek & Krivov 2015), the disc around 49 Ceta is known to host a high amount of gas (e.g. Zuckerman et al. 1995; Hughes et al. 2017, Moór et al., in preparation). The presence of gas might lead to a longer residence time of sub-blow-out grains

produced by collisions, so we would expect an increased number of small grains (Kral et al. 2018). However, we found the surface brightness to be rather weak in scattered light, speaking against this assumption.

A reason for a possible lack of small particles might be provided by the blow-out limit for pure astronomical silicate, showing that grains smaller than $3\ \mu\text{m}$ are expelled from the 49 Ceti system (Burns, Lamy & Soter 1979; Bohren & Huffman 1983). Fig. A2 shows that grains smaller than $1\ \mu\text{m}$ possess the highest scattering efficiency. For larger grains this parameter stays nearly constant and thus, the scattered light is mainly determined by the particle cross-section, which is decreasing with increasing particle size, assuming a power-law size distribution (e.g. Dohnanyi 1969). Furthermore, considering the inclined disc of 49 Ceti, grains larger than $3.5\ \mu\text{m}$ are not contributing as effectively to the scattered light as smaller particles at the observational wavelength used (Zubko 2013).

Another possibility for the lack of small grains is a dynamically ‘cold’ disc where an imbalance between the particles’ production and destruction rate leads to a natural depletion of grains up to a few times the blow-out size (see fig. 7 of Thébaud & Wu 2008). Furthermore small-grain depletion might be caused by the surface energy conservation criterion suggested by Krijt & Kama (2014). Here, the minimum collisional fragment size is determined by the energy necessary to form the small grains. Never the less, the aforementioned mechanisms seem to be negligible for discs around A-type host stars (Thebaud 2016).

Thus, the explanation of a low surface brightness due to a broad on-sky area of the disc might be more appropriate than a lack of small grains, although further studies are needed to confirm this suspicion.

6.3 Model images

6.3.1 Thermal emission

Considering the thermal emission maps we found elongated residuals in the outer disc region for the single-power-law profile including a narrow ring and the double-power-law profile, which can be explained in different ways. First, they might be modelling artefacts since for the single-power-law model without a ring these extended residuals are not visible. Secondly, the observations might suggest that there is a higher amount of grains in several parts of the outer disc than provided by the models. We do not see a symmetric distribution such as ring-shaped residuals and thus, it is possible that the higher amount of particles is caused by recent collisions between massive bodies (Olofsson et al. 2016) or stirring effects, such as self-stirring (e.g. Wyatt 2008; Kennedy & Wyatt 2010) or planetary stirring (e.g. Mustill & Wyatt 2009), although there were no planets found in the 49 Ceti system so far (Choquet et al. 2017).

Besides the dust-stirring mechanisms, the particles might be dragged outwards by present gas (e.g. Takeuchi & Artymowicz 2001; Thébaud & Augereau 2005; Krivov et al. 2009; Kral et al. 2018, Moór et al., submitted). Never the less, the influence of the gas on dust particles may be limited to the smallest grains ($< 5\ \mu\text{m}$) not sensitively traced at sub-millimetre wavelengths.

6.3.2 Scattered light

Comparing the scattered light maps to our ADI-reduced image we found that the double-power-law model reproduces the observations best. However, residuals along the semimajor axis can be found in all residual images, but due to the complex artefact structure the

remaining scattered light is of the order of the noise level that was estimated for the disc.

In all semidynamical models applied to the scattered light observations, the grain size distribution inferred from SED fitting was used. Here, a minimum grain size of $5.14\ \mu\text{m}$ was assumed while the blow-out grain size for 49 Ceti lies at $2.9\ \mu\text{m}$ using pure astronomical silicate. The grains between 2.9 and $5.14\ \mu\text{m}$ move on bound orbits around their host star and would therefore significantly contribute to the flux density in scattered light if they were present in the disc.

Thus, we generated an additional model assuming the best-fitting parameters of the single-power-law radial profile ($p = 0.6$) and a size distribution ranging from the blow-out grain size of $2.9\ \mu\text{m}$ to the upper cut-off size of $15\ \mu\text{m}$. The result can be seen in Fig. 13.

As suspected, the highly eccentric grains lead to a broader dust distribution and thus, the flux density in the outer disc regions increases comparably to the model using $5.14\ \mu\text{m}$ as minimum grain size. Furthermore, the forward scattering becomes stronger, so the disc signal is overestimated close to the star, leading to an increased χ_{red}^2 of 2.27 in comparison to the models using the SED size distribution where we found $\chi_{\text{red}}^2 = 2.11$. In an extended study we analysed scattered light models using a grid of different minimum grain sizes between the blow-out limit ($2.9\ \mu\text{m}$) and the best-fitting size of the SED ($5.14\ \mu\text{m}$). The model using a size of $5\ \mu\text{m}$ delivers the best result, with $\chi_{\text{red}}^2 = 2.11$. Thus, the semidynamical models give us an additional opportunity to estimate the minimum dust grain size besides a pure SED fit.

6.4 Scattering properties and impact on our results

An explanation for the residuals, although being close to the estimated noise level, might be given by the simplified model assumption considering the dust grains to be compact spheres in order to use Mie theory. It is well established that the optical properties, such as absorption and scattering efficiencies or the asymmetry parameter, strongly depend on the particle shape, which can lead to significant deviations from the Mie values assumed (e.g. Schuerman et al. 1981; Weiss-Wrana 1983; Mugnai & Wiscombe 1986). Hence, in comparison to non-spherical grains, the Mie theory approach overestimates the fraction of forward scattering for larger particles (e.g. Arnold et al. 2018). In order to stay in an appropriate grain size regime, we estimated an upper cut-off grain size of $15\ \mu\text{m}$ for particles still significantly contributing to the measured scattered light and omitted all larger particles (see Section 4.3; Zubko 2013).

To weaken the effect of forward scattering, many debris disc studies use the HG approach (Henyey & Greenstein 1941), where the asymmetry parameter, g , is fixed to a specific value between -1 and 1 to give an integrated scattering phase function independent of particle composition and sizes.

In the first scattered light study of 49 Ceti, Choquet et al. (2016) gave a best-fitting value of $g = 0.1$. To check whether the remaining emission is caused by the overestimation of forward scattering, we calculated a set of models based on the single-power-law radial distribution and fixed the asymmetry parameter for each fiducial disc. In this approach, the g parameter is varied between -0.9 and 0.9 in steps of 0.1 . We found a best-fitting model with $g = 0.1$, which is in agreement with Choquet et al. (2017). The result is shown in Fig. 14.

Since the amount of forward scattering is reduced in the HG approach, we could reduce the overestimation of scattered light close to the star. Never the less, due to the higher particle eccentric-

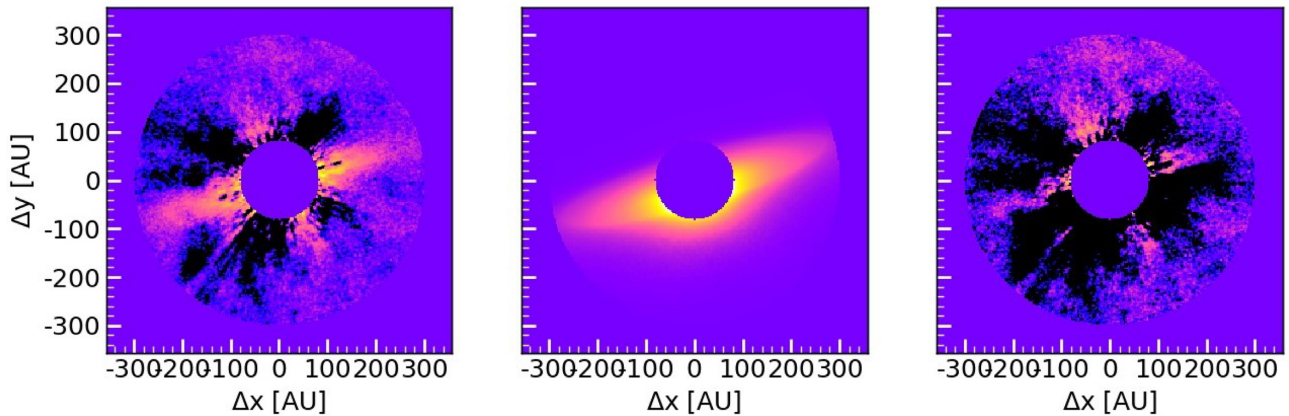


Figure 13. Same as Fig. 10, using the double-power-law radial profile and a size distribution between 2.9 and 15 μm . The radial distribution index is $p = 0.6$.

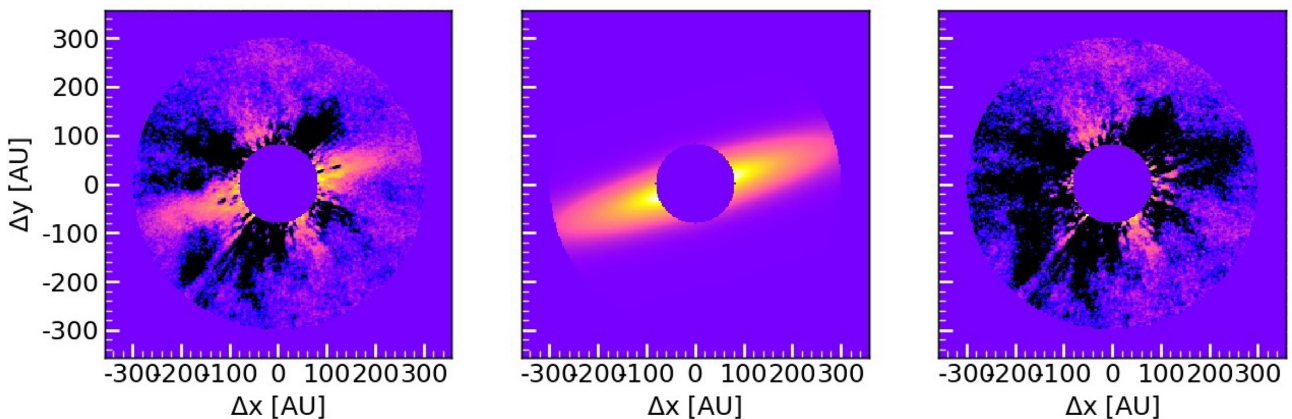


Figure 14. Same as Fig. 10, using the single-power-law radial profile with a fixed asymmetry parameter of $g = 0.1$.

ities (see Appendix B for more details) in comparison to the discs assuming Mie theory, we get an overestimation of flux density in the outer disc region by assuming the radial distribution index to be $p = 0.6$.

At this point, we have to provide a word of caution about the usage of the HG approach together with our semidynamical dust modelling since it is an approach often used in former studies (e.g. Esposito et al. 2016; Lee & Chiang 2016; Olofsson et al. 2016). The MODERATO code uses Mie theory to calculate the optical parameters of the generated dust grains. However, it also serves as a basis to compute the radiation pressure parameter, β (see equation A1), and therefore the dust particle orbits. It could be shown that β depends as strongly on the shape of the dust grains as the optical parameters and thus can easily differ by 75 percent comparing equivalent surface areas of non-spherical and spherical grains (e.g. Schuerman et al. 1981). By fixing the asymmetry parameter, the optical properties of the dust material assumed are tampered and hence, using the HG approach is inconsistent with the dust population inferred from Mie theory. Furthermore, to calculate the flux density of the scattered light not only the asymmetry parameter but also the scattering and extinction efficiencies are needed. These parameters are not provided by the HG approach and thus have to be taken from Mie calculations or comparable methods, which enlarges the already existing inconsistency. A more detailed comparison between the HG approach and Mie theory can be found in Appendix B.

In contrast to Mie and HG theory, a more sophisticated approach to model the scattered light might be given in the discrete dipole approximation (e.g. Draine & Flatau 2013).

7 SUMMARY

We performed a multiwavelength study of the debris disc around 49 Ceti focusing on the dust component. We presented new scattered light data obtained with the SPHERE/IRDIS instrument on the VLT in H23 dual band and Y-band filters and used thermal emission data from a former ALMA study at 850 μm . The H23-band detection was weak in comparison to the Y-band data, so we focused our analysis on the Y-band data. For future SPHERE observations of comparable debris discs we therefore suggest using a broad-band filter for stronger detections.

In both wavelength regimes the disc radius was found to be ~ 280 au. While for the ALMA detection a clear decrease in surface brightness could be observed, the extent of the disc in scattered light is limited by the noise level and might therefore be underestimated.

In a first modelling step, we fitted the SED of 49 Ceti to obtain information on the grain size distribution. We inferred a dominant particle radius of 5.14 μm and a size distribution index of 3.77, suggesting that the disc is dynamically excited.

We computed semidynamical models using three different radial surface density profiles. By comparing our models to the observations in thermal emission and scattered light, we found that all

three can reproduce both SPHERE and ALMA observations, but that the double-power-law profile achieves the best-fitting results. Hence, we assume that the small grains ($\sim 5 \mu\text{m}$) dominant in scattered light and the large particles dominant in thermal emission stem from the same planetesimal belt and are mainly influenced by radiation pressure and collisions. Since transport processes, such as Poynting–Robertson drag, have greater effect on small particles we would expect differences in the radial dust distribution of small and large grains. However, these differences might only be observable in the inner disc region between the planetesimal belt and the star (Kennedy & Piette 2015). Since our observations are not sensitive for this inner region of the 49 Ceti debris disc we cannot draw any conclusions on such inward-directed transport processes.

ACKNOWLEDGEMENTS

Based on observations collected at the European Southern Observatory under ESO programmes 198.C–0209(N) and 097.C–0747(A).

NP is thankful for fruitful discussions with Torsten Löhne and Alexander Krivov. AM acknowledges support from the Hungarian National Research, Development and Innovation Office NKFIH Grant KH-130526. JO acknowledges financial support from the ICM (Iniciativa Científica Milenio) via the Núcleo Milenio de Formación Planetaria grant, from the Universidad de Valparaíso, and from Fondecyt (grant 1180395) This project has received funding from the European Research Council (ERC) under the European Union’s Horizon 2020 research and innovation programme under grant agreement No 716155 (SACCRED). FMe acknowledges funding from ANR of France under contract number ANR-16-CE31-0013. AZ acknowledges support from the CONICYT + PAI/Convocatoria nacional subvención a la instalación en la academia, convocatoria 2017+Folio PAI77170087. This work has made use of data from the European Space Agency (ESA) mission *Gaia* (<https://www.cosmos.esa.int/gaia>), processed by the *Gaia* Data Processing and Analysis Consortium (DPAC, <https://www.cosmos.esa.int/web/gaia/dpac/consortium>). Funding for the DPAC has been provided by national institutions, in particular the institutions participating in the *Gaia* Multilateral Agreement. SPHERE is an instrument designed and built by a consortium consisting of IPAG (Grenoble, France), MPIA (Heidelberg, Germany), LAM (Marseille, France), LESIA (Paris, France), Laboratoire Lagrange (Nice, France), INAF-Osservatorio di Padova (Italy), Observatoire de Genève (Switzerland), ETH Zurich (Switzerland), NOVA (Netherlands), ONERA (France), and ASTRON (Netherlands) in collaboration with the ESO. SPHERE was funded by the ESO, with additional contributions from CNRS (France), MPIA (Germany), INAF (Italy), FINES (Switzerland), and NOVA (Netherlands). SPHERE also received funding from the European Commission Sixth and Seventh Framework Programmes as part of the Optical Infrared Coordination Network for Astronomy (OPTICON) under grant number RII3-Ct-2004-001566 for FP6 (2004–2008), grant number 226604 for FP7 (2009–2012), and grant number 312430 for FP7 (2013–2016). We also acknowledge financial support from the Programme National de Planétologie (PNP) and the Programme National de Physique Stellaire (PNPS) of the CNRS-INSU in France. This work has also been supported by a grant from the French Labex OSUG@2020 (Investissements d’avenir – ANR10 LABX56). The project is supported by the CNRS, by the Agence Nationale de la Recherche (ANR-14-CE33-0018). It has also been carried out within the frame of the National Centre for Competence in Research PlanetS supported by the Swiss National Science Foundation (SNSF). MRM, HMS, and SD are pleased to

acknowledge this financial support of the SNSF. Finally, this work has made use of the SPHERE Data Centre, jointly operated by OSUG/IPAG (Grenoble), PYTHEAS/LAM/CESAM (Marseille), OCA/Lagrange (Nice), and Observatoire de Paris/LESIA (Paris) and is supported by a grant from Labex OSUG@2020 (Investissements d’avenir – ANR10 LABX56). We thank P. Delorme and E. Lagadec (SPHERE Data Centre) for their efficient help during the data reduction process.

REFERENCES

- Alexander R. D., Clarke C. J., Pringle J. E., 2006, *MNRAS*, 369, 229
 Arnold J. A., Weinberger A., Zubko E., Videa G., 2018, AAS/Division for Planetary Sciences Meeting Abstracts #50, p. 113.12
 Augereau J. C., Nelson R. P., Lagrange A. M., Papaloizou J. C. B., Mouillet D., 2001, *A&A*, 370, 447
 Bailer-Jones C. A. L., Rybizki J., Fouesneau M., Mantelet G., Andrae R., 2018, *AJ*, 156, 58
 Ballering N. P., Rieke G. H., Su K. Y. L., Montiel E., 2013, *ApJ*, 775, 55
 Ballering N. P., Su K. Y. L., Rieke G. H., Gáspár A., 2016, *ApJ*, 823, 108
 Beckwith S. V. W., Henning T., Nakagawa Y., 2000, in Mannings V., Boss A. P., Russell S. S., eds, *Protostars and Planets IV*, University of Arizona Press, Tucson, p. 533
 Beuzit J.-L. et al., 2019, preprint ([arXiv:1902.04080](https://arxiv.org/abs/1902.04080))
 Bockelée-Morvan D., André P., Colom P., Colas F., Crovisier J., Despois D., Jorda L., 1994, in Ferlet R., Vidal-Madjar A., eds, *Proceedings of the 10th IAP Astrophysics Meeting, Circumstellar Dust Disks and Planet Formation*. Institut d’Astrophysique, Paris, p. 341
 Bohren C. F., Huffman D. R., 1983, *Absorption and Scattering of Light by Small Particles*. Wiley and Sons, New York
 Brott I., Hauschildt P. H., 2005, in Turon C., O’Flaherty K. S., Perryman M. A. C., eds, *Proceedings of the Gaia Symposium, ESA SP Vol. 576, the Three-Dimensional Universe with Gaia*, p. 565
 Burns J. A., Lamy P. L., Soter S., 1979, *Icarus*, 40, 1
 Carillet M. et al., 2011, *Exp. Astron.*, 30, 39
 Chen C. H., Mittal T., Kuchner M., Forrest W. J., Lisse C. M., Manoj P., Sargent B. A., Watson D. M., 2014, *ApJS*, 211, 25
 Choquet É. et al., 2016, *ApJ*, 817, L2
 Choquet É. et al., 2017, *ApJ*, 834, L12
 Delorme P. et al., 2017, in Reylé C., Di Matteo P., Herpin F., Lagadec E., Lançon A., Meliani Z., Royer F., eds, *SF2A-2017: Proceedings of the Annual Meeting of the French Society of Astronomy and Astrophysics, held 4-7 July, 2017 in Paris*, p. 347
 Dent W. R. F., Walker H. J., Holland W. S., Greaves J. S., 2000, *MNRAS*, 314, 702
 Dohlen K., Saisse M., Origine A., Moreaux G., Fabron C., Zamkotsian F., Lanzoni P., Lemarquis F., 2008, in *Proc. SPIE Conf. Ser. Vol. 7018, Advanced Optical and Mechanical Technologies in Telescopes and Instrumentation*. SPIE, Bellingham, p. 701859
 Dohnanyi J. S., 1969, *J. Geophys. Res.*, 74, 2531
 Dominik C., Decin G., 2003, *ApJ*, 598, 626
 Donaldson J. K., Lebreton J., Roberge A., Augereau J.-C., Krivov A. V., 2013, *ApJ*, 772, 17
 Draine B. T., 2003, *ARA&A*, 41, 241
 Draine B. T., Flatau P. J., 2013, preprint ([arXiv:1305.6497](https://arxiv.org/abs/1305.6497))
 Engler N. et al., 2017, *A&A*, 607, A90
 Engler N. et al., 2019, *A&A*, 622, 192
 Ertel S., Wolf S., Metchev S., Schneider G., Carpenter J. M., Meyer M. R., Hillenbrand L. A., Silverstone M. D., 2011, *A&A*, 533, A132
 Esposito T. M. et al., 2016, *AJ*, 152, 85
 Fedele D., van den Ancker M. E., Henning T., Jayawardhana R., Oliveira J. M., 2010, *A&A*, 510, A72
 Gaia Collaboration, 2016, *A&A*, 595, A1
 Gaia Collaboration, 2018, *A&A*, 616, A1
 Galicher R. et al., 2018, *A&A*, 615, A92
 Gáspár A., Psaltis D., Rieke G. H., Özel F., 2012, *ApJ*, 754, 74
 Henyey L. G., Greenstein J. L., 1941, *ApJ*, 93, 70

- Higuchi A. E. et al., 2017, *ApJ*, 839, L14
Holland W. S. et al., 1998, *Nature*, 392, 788
Holland W. S. et al., 2017, *MNRAS*, 470, 3606
/mnras/stx1378
Hughes A. M. et al., 2017, *ApJ*, 839, 86
Hughes A. M., Duchêne G., Matthews B. C., 2018, *ARA&A*, 56, 541
Høg E. et al., 2000, *A&A*, 355, L27
Jayawardhana R., Fisher R. S., Telesco C. M., Piña R. K., Barrado y Navascués D., Hartmann L. W., Fazio G. G., 2001, *AJ*, 122, 2047
Jura M., Zuckerman B., Becklin E. E., Smith R. C., 1993, *ApJ*, 418, L37
Kalas P., Graham J. R., Clampin M., 2005, *Nature*, 435, 1067
Kass R. E., Raftery A. E., 1995, *J. Am. Stat. Assoc.*, 90, 773
Kennedy G. M., Piette A., 2015, *MNRAS*, 449, 2304
Kennedy G. M., Wyatt M. C., 2010, *MNRAS*, 405, 1253
Kóspál Á. et al., 2013, *ApJ*, 776, 77
Kral Q., Thébault P., Charoz S., 2013, *A&A*, 558, A121
Kral Q., Matrà L., Wyatt M. C., Kennedy G. M., 2017, *MNRAS*, 469, 521
Kral Q., Marino S., Wyatt M. C., Kama M., Matrà L., 2018, preprint (arXiv: 1811.08439)
Krijt S., Kama M., 2014, *A&A*, 566, L2
Krivov A. V., 2010, *Res. Astron. Astrophys.*, 10, 383
Krivov A. V., Löhne T., Sremčević M., 2006, *A&A*, 455, 509
Krivov A. V., Herrmann F., Brandeker A., Thébault P., 2009, *A&A*, 507, 1503
Lagrange A.-M. et al., 2012, *A&A*, 542, A40
/0004-6361/201118274
Lebreton J., Beichman C., Bryden G., Defrère D., Mennesson B., Millan-Gabet R., Boccaletti A., 2016, *ApJ*, 817, 165
Lee E. J., Chiang E., 2016, *ApJ*, 827, 125
/0004-637X/827/2/125
Löhne T., Krivov A. V., Rodmann J., 2008, *ApJ*, 673, 1123
Löhne T., Krivov A. V., Kirchsclager F., Sende J. A., Wolf S., 2017, *A&A*, 605, A7
Lynden-Bell D., Pringle J. E., 1974, *MNRAS*, 168, 603
MacGregor M. A. et al., 2016, *ApJ*, 823, 79
Maire A.-L. et al., 2016, in Proc. SPIE Conf. Ser. Vol. 9908, Ground-based and Airborne Instrumentation for Astronomy VI. SPIE, Bellingham, p. 990834
Marois C., Lafrenière D., Doyon R., Macintosh B., Nadeau D., 2006, *ApJ*, 641, 556
Martinez P., Dorrer C., Aller Carpentier E., Kasper M., Boccaletti A., Dohlen K., Yaitskova N., 2009, *A&A*, 495, 363
McGuire A. F., Hapke B. W., 1995, *Icarus*, 113, 134
Miles B. E., Roberge A., Welsh B., 2016, *ApJ*, 824, 126
Millar-Blanchaer M. A. et al., 2015, *ApJ*, 811, 18
Milli J. et al., 2014, *A&A*, 566, A91
Milli J., Mouillet D., Lagrange A. M., Boccaletti A., Mawet D., Chauvin G., Bonnefoy M., 2012, *A&A*, 545, A111
Moór A. et al., 2015, *MNRAS*, 447, 577
Mugnai A., Wiscombe W. J., 1986, *Appl. Opt.*, 25, 1235
Mustill A. J., Wyatt M. C., 2009, *MNRAS*, 399, 1403
Neugebauer G. et al., 1984, *ApJ*, 278, L1
Nhung P. T., Hoai D. T., Tuan-Anh P., Diep P. N., Phuong N. T., Thao N. T., Darriulat P., 2017, *MNRAS*, 469, 4726
Olofsson J. et al., 2016, *A&A*, 591, A108
Pawellek N., 2017, PhD thesis, Friedrich Schiller University Jena, Germany, Available at: https://www.db-thueringen.de/receive/dbt_mods_00031595
Pawellek N., Krivov A. V., 2015, *MNRAS*, 454, 3207
Pawellek N., Krivov A. V., Marshall J. P., Montesinos B., Abraham P., Moór A., Bryden G., Eiroa C., 2014, *ApJ*, 792, 65
Roberge A. et al., 2013, *ApJ*, 771, 69
Roberge A., Welsh B. Y., Kamp I., Weinberger A. J., Grady C. A., 2014, *ApJ*, 796, L11
Sadakane K., Nishida M., 1986, *PASP*, 98, 685
Schneider G. et al., 2006, *ApJ*, 650, 414
Schuerman D. W., Wang R. T., Gustafson B. Å. S., Schaefer R. W., 1981, *Appl. Opt.*, 20, 4039
Schüppler C. et al., 2015, *A&A*, 581, A97
Strubbe L. E., Chiang E. I., 2006, *ApJ*, 648, 652
Takeuchi T., Artymowicz P., 2001, *ApJ*, 557, 990
Thalmann C. et al., 2013, *ApJ*, 763, L29
Thebault P., 2016, *A&A*, 587, A88
Thébault P., Augereau J.-C., 2005, *A&A*, 437, 141
Thébault P., Augereau J.-C., 2007, *A&A*, 472, 169
Thébault P., Wu Y., 2008, *A&A*, 481, 713
Torres C. A. O., Quast G. R., Melo C. H. F., Sterzik M. F., 2008, *Young Nearby Loose Associations*. p. 757
Wahhaj Z., Koerner D. W., Sargent A. I., 2007, *ApJ*, 661, 368
Wahhaj Z. et al., 2016, *A&A*, 596, L4
Weiss-Wrana K., 1983, *A&A*, 126, 240
Wright E. L. et al., 2010, *AJ*, 140, 1868
Wyatt M. C., 2005, *A&A*, 433, 1007
Wyatt M. C., 2008, *ARA&A*, 46, 339
Wyatt M. C., Dermott S. F., Telesco C. M., Fisher R. S., Grogan K., Holmes E. K., Piña R. K., 1999, *ApJ*, 527, 918
Zubko E., 2013, *Earth Planets Space*, 65, 139
Zuckerman B., 2019, *ApJ*, 870, 27
Zuckerman B., Song I., 2012, *ApJ*, 758, 77
Zuckerman B., Forveille T., Kastner J. H., 1995, *Nature*, 373, 494
Zuckerman B., Melis C., Rhee J. H., Schneider A., Song I., 2012, *ApJ*, 752, 58

APPENDIX A: THEORETICAL BACKGROUND

The orbits of dust particles are altered by different mechanisms, such as collisions and Poynting–Robertson drag, and stellar radiation pressure is one of the strongest processes.

A1 Radiation pressure

As shown in earlier studies (e.g. Burns et al. 1979; Wyatt et al. 1999) the orbital parameters depend on the radiation pressure parameter, β , given as

$$\beta \equiv \frac{|\vec{F}_{\text{rad}}|}{|\vec{F}_{\text{G}}|} = \frac{3L_{\text{star}}}{16\pi GcM_{\text{star}}} \frac{\bar{Q}_{\text{pr}}}{\rho s}. \quad (\text{A1})$$

Here, L_{star} and M_{star} are the stellar luminosity and mass, G the gravitational constant, c the speed of light, \bar{Q}_{pr} the radiation pressure efficiency averaged over the stellar spectrum, ρ the bulk density of the dust material, and s the grain radius. If we assume a dust particle is released from a planetesimal possessing the orbital parameters semimajor axis, a_p , eccentricity, e_p , and true anomaly, f_p , then the orbit parameters of the dust grain can be calculated with

$$a_d = \frac{a_p(1-\beta)(1-e_p^2)}{1-e_p^2-2\beta(1+e_p\cos(f_p))} \quad (\text{A2})$$

$$e_d^2 = \frac{\beta^2 + e_p^2 + 2\beta e_p \cos(f_p)}{(1-\beta)^2} \quad (\text{A3})$$

$$\tan(\varpi - \varpi_p) = \frac{\beta \sin(f_p)}{\beta \cos(f_p) + e_p}, \quad (\text{A4})$$

where ϖ is the longitude of pericentre. To compute the β parameter, we calculate \bar{Q}_{pr} using Mie theory, where the particles are assumed to be compact spheres (Bohren & Huffman 1983).

In Fig. A1 on the left-hand side the β parameter is shown as a function of grain size. To calculate β , we use the stellar properties of

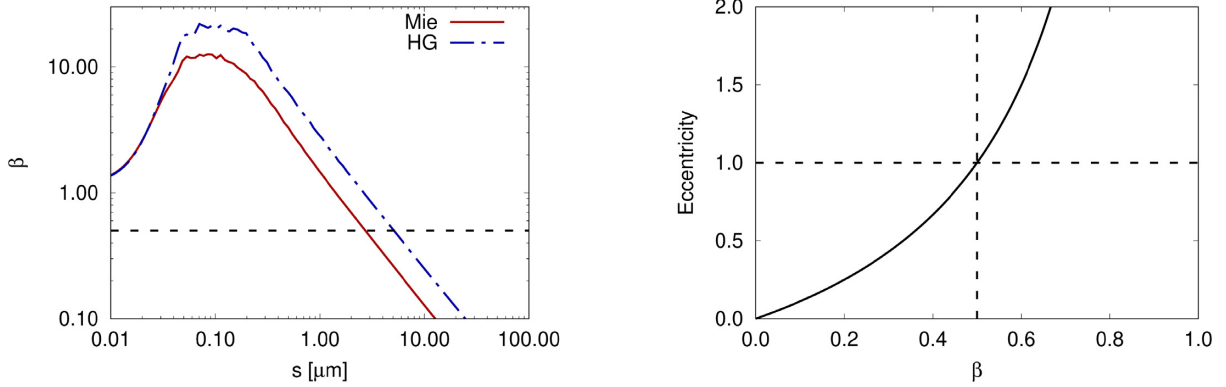


Figure A1. Left: radiation pressure parameter as a function of grain size calculated for 49 Ceti (solid black line). Solid red line: using Mie theory; dash-dotted blue line: using Henyey–Greenstein approach with $g = 0.1$; the black dashed line shows $\beta = 0.5$. Right: particle eccentricity as a function of the radiation pressure parameter (solid black line) assuming a circular orbit for the parent body. The dashed lines show $\beta = 0.5$ and $e = 1.0$.

49 Ceti and astronomical silicate (Draine 2003) with a bulk density of 3.3 g cm^{-3} . On the right-hand side the particle eccentricity is given as a function of β . We use equation (A3) and assume e_p and f_p to be equal to zero. In this case, the eccentricity turns 1 when β is 0.5 and thus, grains below a value of $\beta = 0.5$ stay in bound orbits around the star, while for values larger than 0.5 the particles are expelled from the stellar system on either parabola or hyperbola orbits. In general, β is increasing with decreasing grain size. Therefore, the so-called blow-out grain size for 49 Ceti is $2.9 \text{ }\mu\text{m}$, meaning that grains smaller than this value are expelled from the stellar system.

Furthermore, the smaller the grains the larger the eccentricity gets. As a consequence, small grains spend more time in the apocentre region compared to large particles and thus, it is expected that by tracing small grains in observations we would see larger disc radii than by tracing large grains.

To calculate the dust disc we generate at first the parent belt using the surface number density. In many cases a size-independent power law is assumed:

$$N(r) = N_0 \times \left(\frac{r}{r_0}\right)^{-p}, \quad (\text{A5})$$

where the parameters are the same as described in Section 4.2. Now we have a population of planetesimals at different radii and angles releasing the dust grains. The planetesimals give us the parameters necessary (a_p , e_p , f_p) to calculate the particle orbits (a_d , e_d).

A2 Tracing different grain sizes

It is necessary to investigate the absorption and scattering efficiencies for each grain size and wavelength to get information on the emission of the particles. For thermal emission the absorption efficiency of the grains is of importance, while for scattered light emission it is the scattering efficiency. In Fig. A2 the absorption efficiency is depicted for a wavelength of $850 \text{ }\mu\text{m}$ and the scattering efficiency for $1.04 \text{ }\mu\text{m}$. These are the wavelengths used by SPHERE and ALMA for the 49 Ceti observations used in this study. Grains with a size of $\sim 0.5 \text{ }\mu\text{m}$ possess the highest scattering efficiency while $\sim 200\text{-}\mu\text{m}$ -sized particles show the largest absorption efficiency at the observed wavelengths. This means, we would expect to trace the small grains best with scattered light emission in the near-infrared and the large grains with thermal emission in the sub-millimetre region. However, taking the radiation pressure

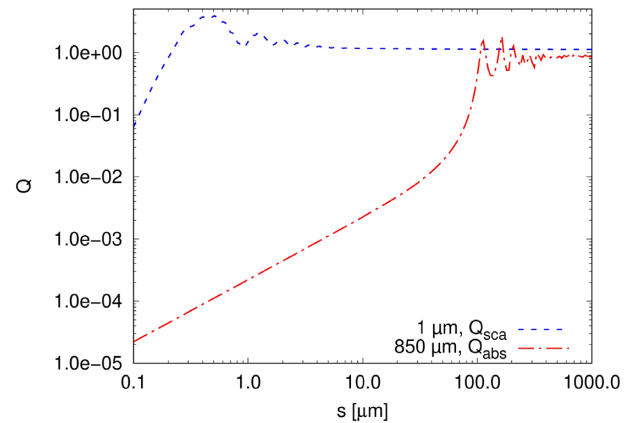


Figure A2. Scattering and absorption efficiency as a function of grain size. The blue dashed line shows the scattering efficiency at a wavelength of $1.04 \text{ }\mu\text{m}$ and the red dash-dotted line the absorption efficiency at $850 \text{ }\mu\text{m}$. The dust composition is pure astronomical silicate.

into account, we expect to see grains larger than the blow-out size.

In Fig. A3 fiducial discs are given for thermal emission and scattered light. We use 1.04 and $850 \text{ }\mu\text{m}$ as observational wavelengths. Furthermore, we assume two cases. The first is that all discs possess the same mass and the second that all discs contain the same number of particles. The scattered light images at $1.04 \text{ }\mu\text{m}$ are shown in the first two rows, where the first row represents discs of the same mass and the second row discs with the same particle number. We see in the first case that the discs get fainter for an increase in grain size and decrease in radius. The latter fact is mainly caused by stellar radiation pressure. In the second case, where the particle number stays constant the discs get brighter.

One reason is the decreasing scattering efficiency. However, it stays nearly the same for grains larger than $10 \text{ }\mu\text{m}$ and thus, the second reason is the constant disc mass leading to a smaller number of large grains. Another point is that the wavy structure of the emission is caused by the phase function, which depends on the grain size, the observation wavelength, and the scattering angle. Considering the thermal emission images, it is obvious that the disc with dust made of $100 \text{ }\mu\text{m}$ grains possesses the largest emission

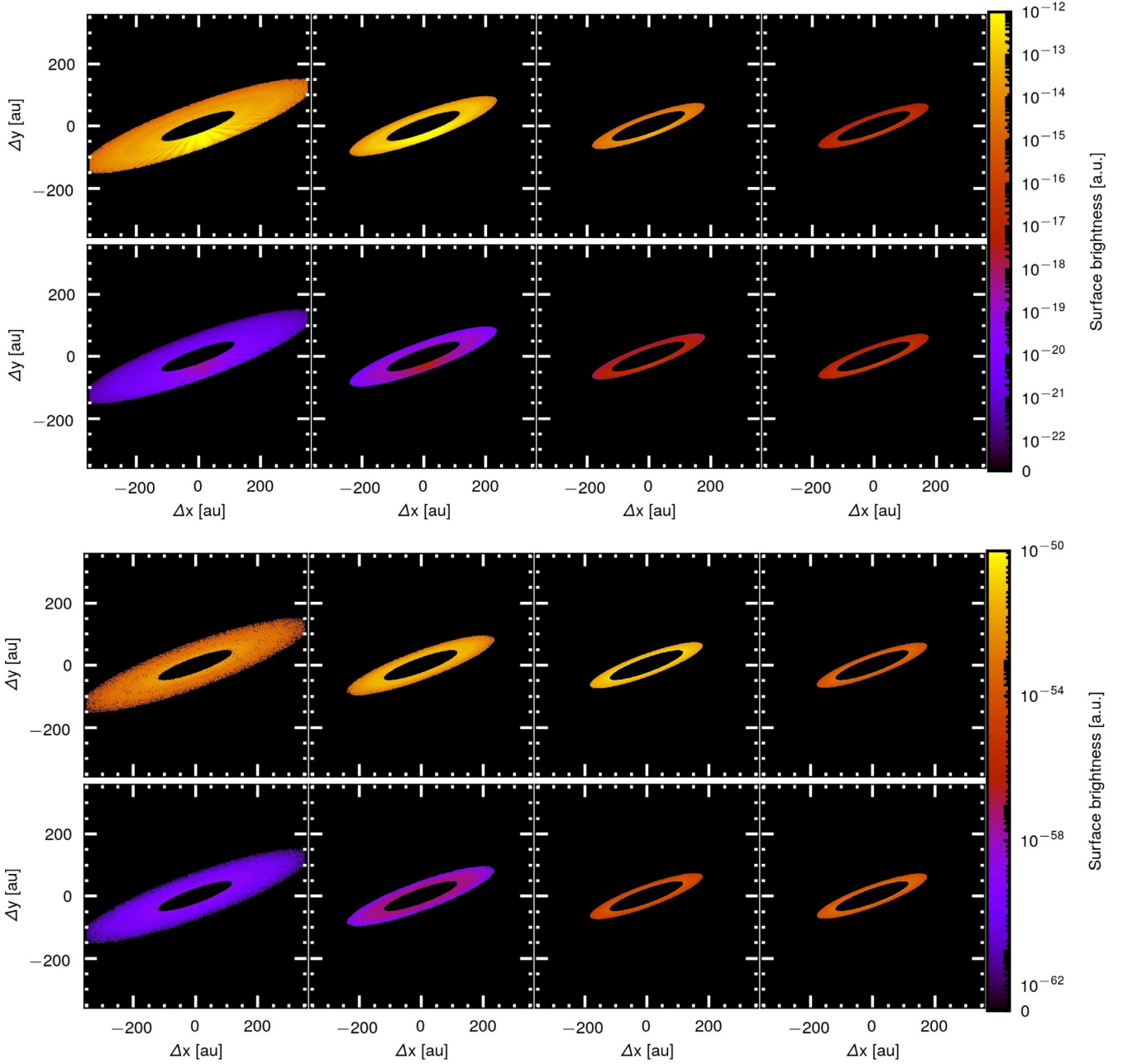


Figure A3. Model discs for different grain sizes. From left to right: the dust is made of a single grain size of 5, 10, 100, 1000 μm . The first row gives the scattering emission of the discs of a constant mass at 1.04 μm . The second row shows the same as the first row, but now the discs have the same number of particles. The third row shows the discs with a constant mass in thermal emission at 850 μm . The bottom row shows the same as the third row, but now the discs have a constant number of particles.

at 850 μm compared to 5, 10, and 1000 μm . The absorption efficiency decreases for particles smaller than 100 μm . Hence, even the larger number of small particles cannot compensate for the lower absorption.

APPENDIX B: COMPARISON OF MIE THEORY AND HENYEY-GREENSTEIN APPROACH

As shown by equation (A1), the radiation pressure parameter, β , is directly proportional to the radiation pressure efficiency, $\overline{Q}_{\text{pr}}(s)$,

averaged over the stellar spectrum which is given by

$$\overline{Q}_{\text{pr}} = \frac{\int Q_{\text{pr}}(s, \lambda) \times F_{\lambda} d\lambda}{\int F_{\lambda} d\lambda}. \quad (\text{B1})$$

Here, Q_{pr} describes the radiation pressure efficiency depending on the grain radius, s , and wavelength, λ , while F_{λ} gives the stellar flux density. For each grain and wavelength, Q_{pr} is calculated by

$$Q_{\text{pr}}(s, \lambda) = Q_{\text{ext}}(s, \lambda) - Q_{\text{sca}}(s, \lambda) \times \langle \cos(\vartheta) \rangle(s, \lambda), \quad (\text{B2})$$

where Q_{ext} and Q_{sca} are the extinction and scattering efficiencies and $\langle \cos(\vartheta) \rangle$ the asymmetry parameter, depending on the scattering angle, ϑ (Bohren & Huffman 1983). This parameter is also called

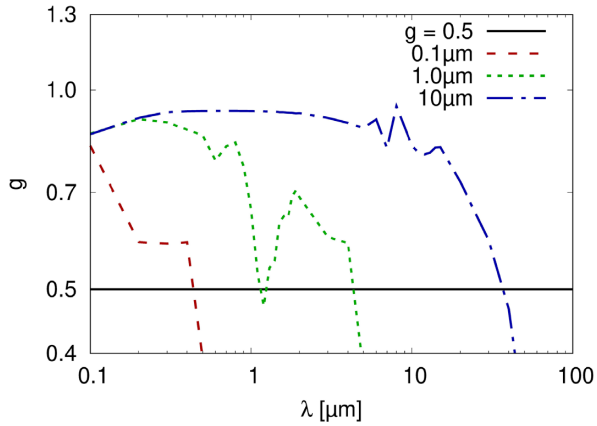


Figure B1. Asymmetry parameter as function of wavelength. Comparison of Mie theory and the Henyey–Greenstein approach using astronomical silicate and a fixed g of 0.5. The black solid line shows the fixed asymmetry parameter; the coloured dashed lines show g for different grain radii (red dashed: 0.1 μm ; green dotted: 1.0 μm ; blue dash-dotted: 10 μm).

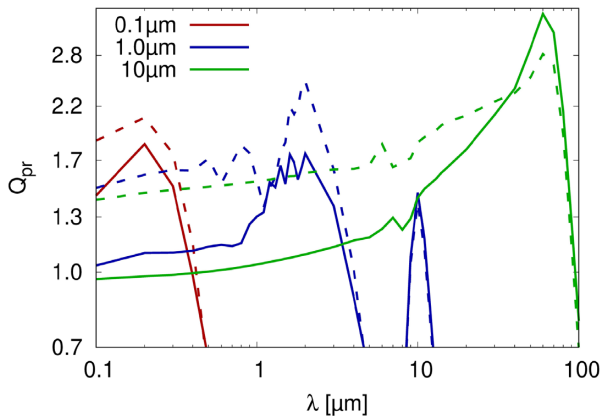


Figure B2. Radiation pressure efficiency as a function of wavelength for the same grain radii as in Fig. B1. The solid lines show the result for Mie theory, the dashed lines for Henyey–Greenstein assuming $g = 0.5$.

g . All the parameters used to calculate Q_{pr} depend on the grain size and the wavelength.

Using the Henyey–Greenstein approach, the asymmetry parameter is fixed and therefore independent of grain size and wavelength, while all other parameters are still calculated by Mie theory or comparable methods. Since the extinction and scattering efficiencies as well as the g parameter depend on the optical constants, i.e. refractive indices, of the dust composition used, the fixation of g resembles a variation of the dust material.

A comparison of g values given by Mie and HG is presented in Fig. B1. Here, g is set to 0.5 resembling a best-fitting value for different studies using the HG approach (e.g. Millar-Blanchaer et al. 2015; Olofsson et al. 2016; Engler et al. 2017, 2018). The values from Mie show strong deviations from this value. For 0.1- μm -sized

particles, g decreases to values close to zero for a wavelength larger than 1 μm while for larger grains this decrease is moved to longer wavelengths.

In Fig. B2 we present the radiation pressure efficiency as a function of wavelength for different grain radii. Depending on the particle size, HG and Mie lead to similar results for wavelengths roughly longer than $\sim 3s$. For shorter wavelengths, the differences between the methods can easily reach 50 per cent, although these deviations decrease for smaller particles (assuming $g = 0.5$).

In the next step we compare the radiation pressure efficiencies averaged over the stellar spectrum for both, HG and Mie (Fig. B3). Here, the value calculated by HG is divided by the value inferred with Mie theory and given as a function of grain radius. Using three different g values between 0.1 and 0.9 for HG, \overline{Q}_{pr} is overestimated for both, $g = 0.1$ and 0.5, with differences of up to ~ 100 per cent assuming $g = 0.1$ and ~ 50 per cent assuming $g = 0.5$. In case of $g = 0.9$, the deviation of \overline{Q}_{pr} is close to zero for grains larger than $\sim 2 \mu\text{m}$ while we underestimate \overline{Q}_{pr} for smaller particles.

The parameter β changes by the same order of magnitude as \overline{Q}_{pr} (see Fig. A1). Hence, similar-sized particles possess different eccentricities for both methods. For example, if we assume a grain with a certain size s for which $\beta = 0.1$ using Mie theory, we get β for HG twice as large assuming $g = 0.1$ (see Figs A1 and B3). This leads to an increase of the particle’s eccentricity by a factor of 2.25 compared to Mie, using equation (A3) and a circular parent belt. For larger β this effect is even stronger due to the non-linear relation between β and grain eccentricity (see Fig. A1). Only for the smallest particles ($s \sim 0.01 \mu\text{m}$) do HG and Mie reach similar values. Hence, by applying the HG approach the dust population inferred with Mie theory is altered by HG.

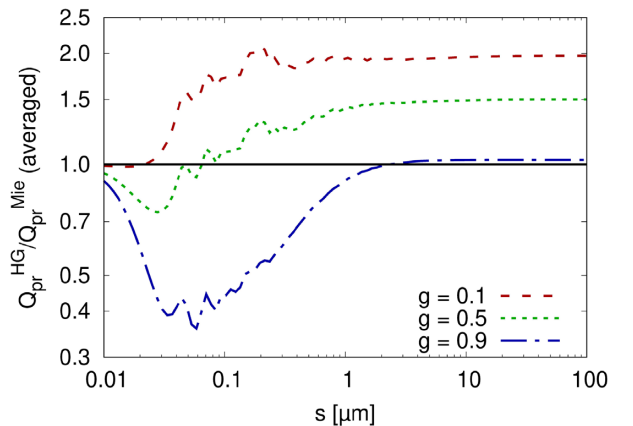


Figure B3. Ratio of the averaged radiation pressure efficiencies of Henyey–Greenstein and Mie theory as a function of grain size for different values of g . Red dashed: $g = 0.1$; green dotted: $g = 0.5$; blue dash-dotted: $g = 0.9$; black solid: ratio of 1.

This paper has been typeset from a \LaTeX file prepared by the author.